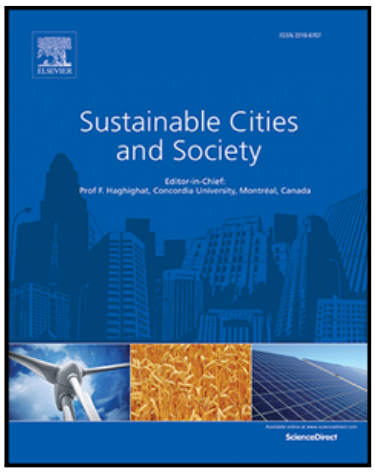

Multi-objective optimization of urban block morphology for thermal comfort and air quality: An integrated CFD-machine learning framework

Meilin Wang , Hang Ma , Xing Zheng , Yi Zhang , Chunze Li , Pengyuan Shen

PII: S2210-6707(25)00793-0
DOI: https://doi.org/10.1016/j.scs.2025.106921
Reference: SCS 106921

To appear in: *Sustainable Cities and Society*

Received date: 30 June 2025
Revised date: 8 September 2025
Accepted date: 19 October 2025

Please cite this article as: Meilin Wang , Hang Ma , Xing Zheng , Yi Zhang , Chunze Li , Pengyuan Shen , Multi-objective optimization of urban block morphology for thermal comfort and air quality: An integrated CFD-machine learning framework, *Sustainable Cities and Society* (2025), doi: https://doi.org/10.1016/j.scs.2025.106921

Highlights

- Two-way coupled CFD model captures thermal-PM2.5 interactions in urban blocks
- RSM achieves 95% accuracy (R^2=0.98-0.99) while reducing computational cost
- Optimal H/W ratios: 0.7-1.0 for low density, 1.3-1.6 for high density zones
- Case study achieves 2.09°C temperature reduction with regulatory compliance

Multi-objective optimization of urban block morphology for thermal comfort and air quality: An integrated CFD-machine learning framework

Meilin Wang[b], Hang Ma[b], Xing Zheng[c], Yi Zhang[a], Chunze Li[a], Pengyuan Shen[a*]

[a] Shenzhen International Graduate School, Tsinghua University, Shenzhen, 518055, China

[b] Harbin Institute of Technology, Shenzhen, 518055, China

[c] Department of Architecture and Civil Engineering, City University of Hong Kong, Kowloon, Hong Kong, China

Abstract

Urban block morphology can influence thermal comfort and air quality, yet existing studies have focused on single environmental objectives. This study develops an integrated optimization framework simultaneously addressing thermal environment and $PM_{2.5}$ concentration through a novel two-way coupled numerical model. Key morphological parameters, including building length, width, height, spacing, and orientation, establish a parametric geometric model of idealized residential blocks. The methodology integrates physics-driven computational fluid dynamics with data-driven response surface modeling and multi-objective genetic algorithms. The two-way coupled model captures interactions between thermal environment and particulate matter dispersion, while Latin Hypercube Sampling generates 200 morphology samples for CFD simulations. Response surface models linking morphology parameters to Universal Thermal Climate Index (UTCI) and $AQI_{PM2.5}$ achieve 95% accuracy (R^2 = 0.98-0.99), enabling efficient optimization. Multi-objective optimization reveals trade-offs between thermal comfort and air quality, yielding Pareto-optimal solutions with distinct parameter ranges for different floor area ratios. Building orientation within 15° of prevailing winds optimizes both objectives, while longitudinal spacing exhibits the strongest influence (correlation ±0.81). Optimal height-to-width ratios range from 0.7-1.0 for low-density to 1.3-1.6 for high-density developments. Case study validation in Shenzhen achieves air temperature reductions up to 2.09°C while maintaining regulatory compliance. The framework provides evidence-based design guidelines for hot-humid climates, offering urban planners practical tools for creating healthier residential environments while balancing development viability and environmental performance.

Keywords: Urban morphology, Thermal environment, Air quality, Multi-objective optimization, Computational fluid dynamics

Nomenclature

Abbreviations	Definition
AQI	Air Quality Index
$AQI_{PM2.5}$	Air Quality Index for $PM_{2.5}$
CFD	Computational Fluid Dynamics
CF	Coverage Factor
DPM	Discrete Phase Model
DO	Discrete Ordinates
DOE	Design of Experiment
FAR	Floor Area Ratio
H/W	Height-to-Width ratio
LHS	Latin Hypercube Sampling
MAE	Mean Absolute Error
MOGA	Multi-Objective Genetic Algorithm
$PM_{2.5}$	Particulate Matter with diameter ≤ 2.5 μm
RANS	Reynolds-Averaged Navier-Stokes
RMSE	Root Mean Square Error
RNG	Renormalization Group
RSM	Response Surface Model/Methodology
SHAP	SHapley Additive exPlanations
SR	Spacing Ratio
UDF	User-Defined Function
UHI	Urban Heat Island
UTCI	Universal Thermal Climate Index
VKT	Vehicle Kilometers Traveled
XGBoost	eXtreme Gradient Boosting

1 Introduction

Rapid global urbanization and climate change have intensified environmental stresses that pose significant threats to energy use, thermal comfort, and public health [1-3]. Urban heat islands and air pollution represent two of the most pressing challenges facing modern cities, with building morphology playing a critical role in mediating both phenomena [4]. Extreme heat exposure causes a spectrum of health impacts ranging from heat exhaustion and dehydration to cardiovascular stress, with vulnerable populations facing elevated morbidity and mortality risks [5], increasing human morbidity and mortality [6, 7]. The severity of these impacts is exemplified by major heat wave events, including the 2003 European heat wave that caused approximately 15,000 deaths in France alone [8] and the 2009 Melbourne heat wave responsible for 374 fatalities over just four days [9]. Concurrently, the accumulation of pollutants in urban boundary layers leads to the occurrence of many diseases [10-12] with serious implications for human health and safety [13, 14]. Ambient air pollution kills 4.2 million people annually [15], indicating air pollution as a major environmental and health problem in many countries [16]. The spatial distribution and concentration of fine particulate matter ($PM_{2.5}$) are strongly influenced by urban morphological characteristics, including building geometry, street configuration, and block layout patterns.

The morphology of urban blocks—including building height, width, orientation, and street layout—significantly influences both the urban thermal environment and the distribution and concentration of $PM_{2.5}$ [17, 18]. These morphological parameters affect solar radiation reception and ventilation efficiency [18], thereby shaping local microclimates. In recent years, rapid urbanization has exacerbated global climate change, urban heat island effects, and air pollution problems [19], highlighting the necessity of balancing thermal environment and air quality in urban design. However, existing studies indicate that urban block morphology exerts dual and sometimes contradictory effects on thermal comfort and $PM_{2.5}$ concentrations [4]. Design strategies that optimize one environmental factor often compromise the other, creating complex trade-offs that current planning approaches inadequately address.

This study develops an integrated optimization framework for residential block morphology that simultaneously addresses thermal comfort and air quality through a novel two-way coupled numerical model. The primary objective is to establish a systematic methodology for optimizing

building morphology parameters that balances the often conflicting requirements of thermal environment improvement and $PM_{2.5}$ concentration reduction. By combining physics-driven computational fluid dynamics with data-driven optimization techniques, this research provides practical design guidance for creating healthier residential environments in hot-humid climates while maintaining development density requirements.

2 Literature Review

2.1 Urban Block Morphology Effects on Thermal Environment and Air Quality

The morphology of urban blocks can influence the reception of solar radiation and ventilation efficiency [20], thereby shaping the thermal environment. An essential parameter in evaluating urban morphology is the height-to-width ratio (H/W) of urban canyons, which is directly linked to thermal comfort. Variations in H/W result in distinct thermal environments: wide urban canyons (H/W < 0.5), balanced urban canyons (H/W = 1), and deep urban canyons (H/W > 2) exhibit markedly different thermal characteristics [21]. During hot summers, deep urban canyons effectively block solar radiation [21] and mitigate unheated airflow [22], leading to lower internal temperatures [23] and more comfortable thermal environments [24]. However, studies have also highlighted conflicting findings—the combination of high-rise buildings with deep urban canyons may reduce wind speed [25], potentially compromising thermal comfort through reduced ventilation and heat removal.

Recent computational advances have enhanced the efficiency of thermal environment assessment. Cui et al. demonstrated that machine learning models, specifically XGBoost with SHAP analysis, can predict pedestrian-level thermal conditions with high accuracy while providing explainable insights into morphological influences [18]. Their findings emphasize the importance of spatial positioning variables over traditional building parameters, suggesting that urban context can affects local thermal environments. This represents a shift from purely geometric considerations to more holistic spatial analyses.

The relationship between urban morphology and air quality presents equally complex dynamics. In deep urban canyons, PM concentrations are considerably higher compared to balanced and wide urban canyons [17]. Elevated temperatures on building surfaces and the ground can further influence particulate diffusion through thermophoretic forces and buoyancy-driven

flows. For instance, in balanced urban canyons with Froude numbers between 0.19 and 0.38, particulate dispersion is enhanced through optimal mixing conditions. However, in deep urban canyons, a clockwise vortex forms above the canyon while a weaker counterclockwise vortex develops within, severely suppressing particulate dispersion [26]. This vortex structure creates a "lid effect" that traps pollutants at pedestrian level, exacerbating exposure risks.

These contradictory findings highlight a fundamental challenge in urban design: compact urban layouts remain widely recommended for thermal comfort [27], as shading is a primary strategy for improving thermal conditions in urban streetscapes [28]. Deep urban canyons can notably lower the physiological equivalent temperature (PET) [23], and implementing effective shading measures within wide urban canyons can also substantially enhance thermal comfort [29]. Conversely, to reduce urban canyon PM concentrations, lower H/W values are recommended [29], creating an inherent conflict between thermal and air quality objectives.

Building orientation represents another vital morphological parameter with dual impacts. The orientation can affect thermal environment by determining solar radiation exposure and wind patterns [30, 31], particularly in deep urban canyons [32]. Strategic building layouts can facilitate mutual shading and self-shading, effectively reducing daytime temperatures [33]. Field measurements by Georgakis and Santamouris revealed temperature differences of up to 14°C between opposing walls of streets during summer [34], while Offerle et al. [35] in Gothenburg, Sweden, showed that for streets with H/W below 0.48, temperature differences of up to 15 □ were observed between street-facing walls and between walls and the surrounding air.

The angular relationship between street axes and prevailing wind directions [36] fundamentally affects both ventilation and pollutant dispersion. When wind flows obliquely to the street axis, a helical vortex forms along the street length [37], while perpendicular wind flow generates either single or dual counter-rotating vortices [38]. Changes in wind direction not only alter the pathways of PM dispersion but also induce turbulence variations that can lead to significant differences in PM concentrations [39]. These flow patterns directly influence PM dispersion pathways—perpendicular winds increase PM concentrations on windward sides while decreasing them on leeward sides [40]. Buccolieri et al. found that perpendicular wind directions reduce canyon wind speeds, resulting in higher PM concentrations, while parallel winds enhance roof-level airflow and turbulence intensity, promoting dispersion [41]. García et al. further

demonstrated that parallel wind directions enhance recirculation within canyons, improving both wind speed and dispersion efficiency [42]. Interestingly, some studies indicate that 45° wind angles provide optimal PM dispersion compared to fully parallel or perpendicular orientations [17], though this finding lacks consensus across different urban contexts.

2.2 Multi-objective Optimization of Urban Block Morphology

Urban morphology, thermal environment, air quality are interconnected in multifaceted and even contradictory ways, which underlines the inadequacy of designing with one goal. Though these studies give very good insights into each specific environmental phenomenon, they do not establish a solution to the main problem urban planners are dealing with: how to optimize several, sometimes competing environmental targets simultaneously. This awareness has also encouraged researchers to look into unified optimization frameworks which can strike a balance between thermal comfort and air quality factors, although these methods are still very early in the literature as the current literature reveals gaps in integrated optimization frameworks. Most existing studies adopt single-objective approaches, optimizing either thermal conditions [18, 43] or air quality [26, 44] in isolation, potentially leading to suboptimal or even counterproductive outcomes for the neglected objective.

Li et al. [45] represent one of the few attempts at simultaneous assessment, evaluating both thermal environments and air quality under varying frontal area densities of buildings. They recommended an optimal range of 0.82 to 0.84 for frontal area density. However, their study notably lacks consideration of the interactive dynamics between thermal environments and air pollutants—treating them as independent phenomena rather than coupled systems. This limitation is critical, as thermal buoyancy affects pollutant dispersion [46], while pollutant concentrations influence radiative transfer and thus thermal conditions [47].

The computational complexity of multi-objective optimization in urban contexts presents another challenge. Traditional CFD approaches, while physically accurate, require substantial computational resources that make iterative optimization impractical [48]. Each simulation may require hours or days of computation time, rendering genetic algorithms or other optimization methods that require thousands of evaluations infeasible [49]. This computational bottleneck has limited most studies to sensitivity analyses rather than true optimization, examining a handful of

scenarios rather than systematically searching the design space [50].

Recent advances in surrogate modeling offer potential solutions. Response surface methodology (RSM) and machine learning approaches can approximate CFD results with sufficient accuracy for optimization purposes while reducing computational time by orders of magnitude [51, 52]. However, these methods have seen limited application in integrated thermal-air quality optimization. Most applications focus on single objectives—either using surrogate models for thermal comfort prediction [18, 53] or for air quality assessment [54], but rarely for simultaneous multi-objective optimization.

The coupling mechanisms between thermal and air quality phenomena remain poorly understood in the optimization context. Two-way coupling, where thermal conditions affect pollutant dispersion through buoyancy and thermophoresis while pollutants influence radiative transfer, has rarely been implemented in optimization studies. Wang et al. recently developed a two-way coupled model demonstrating these interactions, but their work focused on analysis rather than optimization [55]. The absence of coupled models in optimization frameworks represents a critical gap, as it may lead to solutions that appear optimal under decoupled analysis but perform poorly when coupling effects manifest in reality [56].

Furthermore, existing optimization studies typically employ simplified geometric models that may not capture the complexity of real urban environments [57, 58]. Idealized arrays of uniform buildings, while useful for parametric studies, fail to represent the heterogeneity of actual urban blocks. The scalability of optimization results from simplified to realistic geometries remains largely unexplored, raising questions about the practical applicability of published optimization strategies [59]. Constraint handling in multi-objective optimization of urban morphology presents additional challenges inadequately addressed in current literature. Real-world urban design must satisfy multiple constraints including floor area ratios (FAR), building codes, setback requirements, and economic viability [60, 61]. These constraints significantly reduce the feasible design space and may fundamentally alter optimal solutions. However, most optimization studies either ignore these constraints or apply them post-hoc, rather than incorporating them directly into the optimization framework. Moreover, the validation of optimization results against real-world performance represents a critical gap. While individual CFD models may be validated [62], the performance of optimized designs in actual urban environments is rarely verified. This absence of

empirical validation raises questions about the reliability of optimization recommendations and their transferability across different climatic and urban contexts [63, 64].

2.3 Contribution of This Research

According to the identified gaps in the existing literature, this research will be considered in the context of the following main research questions: How do interactive effects between thermal environment and $PM_{2.5}$ dispersion affect optimal morphological parameters, and are they able to be represented by two-way coupling? Is it possible that a CFD-machine learning framework can lead to the development of an accurate model that will have reduced computational needs to be useful in practice? What are the preferable ranges of morphological parameters of various development density, which provide a balance between air quality and thermal comfort? How do UTCI-$AQI_{PM2.5}$ trade-offs appear when solutions that are Pareto-optimal exist on real-world constraints?

The major contributions of this research include: we developed a novel two-way coupled numerical model to describe dynamic coupling between thermal environment and $PM_{2.5}$ dispersion, with consideration of the effects of $PM_{2.5}$ on radiative transfer, and also taking into account thermal buoyancy and thermophoretic forces on particle transport. Secondly, we combined physics-based computationally intensive CFD simulation with data-driven surrogate-based optimization, multi-objective genetic algorithms, and high-level of accuracy, trading off computational time of days, with minutes. Thirdly, we offered quantitative morphological design strategies in hot-humid climates, in which optimal H/W ratios vary by development density (0.7-1.0 for FAR ~3, 1.3-1.6 for FAR ~6) and the orientation of buildings to the prevailing winds. Constrained multi-objective optimization was conducted, in which FAR, building density, and setback requirements were included during the optimization process. Lastly, we made practical applicability by testing it out in Shenzhen by demonstrating temperature reductions and regulatory compliance. The combined effects of these contributions are that they can equip the urban planners with scientifically sound and computationally affordable means to design healthier living environments that will promote thermal comfort and air quality without compromising the viability of development.

3 Methodology

3.1 Overall approach and workflow

In this study, the authors target residential blocks as a typical and most common type of urban block development, especially in the environment of rapid urbanization as a place where residential land use encompasses the largest part of urban space. There are some special optimization complexities associated with residential blocks, considering that buildings need to facilitate comfort to occupants and healthy outdoor resources for community activities. Combining physics-driven numerical simulation calculations with data-driven multi-objective optimization, the complex numerical simulation process is transformed into mathematical relationships, effectively reducing computation time and quickly obtaining output variables for optimization iteration, achieving rapid optimization of urban outdoor space forms. Specifically, physics-driven methods focus on establishing detailed physical models, which can deeply understand the coupling mechanism between thermal environments and fine particulate matter, but they are slow in computation and difficult to optimize quickly. Data-driven methods, based on computational fluid dynamics (CFD) technology and optimization algorithms, store the input and output data of CFD simulations in a dataset, and construct RSM with the dataset, which can effectively handle multiple objectives in complex systems and achieve optimization results. These results can then be verified using CFD simulations. The optimization process of urban residential block morphology based on bidirectional coupling models and multi-objective optimization algorithms is shown in Fig. 1.

(1) First, the stage of constructing and designing variables for the CFD numerical model, which mainly includes the construction of the basic geometric model, the design of variables, and the setup of numerical simulation. Morphology parameters (building length, width, spacing, angle, height) are set as design variables to control the changes in the block geometry. In conjunction with Shenzhen's residential design specifications, the range of parameter changes is set. Outdoor temperature, wind speed, and $PM_{2.5}$ concentration are set as output parameters for CFD simulation. Then, in the CFD module, complete the steps of mesh generation, boundary condition setup, model and solver selection, confirm the parameter set, and carry out simulation calculations.

(2) Next, enter the design of experiment (DOE) and CFD batch simulation phase. By

sampling the morphology design variables, a certain number of uniformly distributed block morphology samples are formed to construct the DOE matrix. Afterward, the samples are simulated one by one according to the CFD calculation plan set in the initial scheme. Then, export the output parameters and calculate the universal thermal climate index (UTCI) and air quality index of $PM_{2.5}$ ($AQI_{PM2.5}$). Merge the input parameters with the new output parameters (UTCI and $AQI_{PM2.5}$) into a new DOE matrix and import it into the dataset.

(3) Based on the DOE matrix, apply interpolation algorithms to fit the input variables and output parameters, creating an RSM. Verify the prediction accuracy of the RSM; if it meets the accuracy requirements, proceed to the optimization process; if not, redo the experimental design and follow the above process for a new RSM construction until the accuracy requirements are met.

(4) Finally, use a multi-objective genetic algorithm to call the RSM for optimization iteration. Under the two objective functions of the lowest UTCI and $AQI_{PM2.5}$, find the optimal solution set and compare the optimized solution with the CFD simulation results. Select the best range of morphology parameters for residential blocks to provide a scientific reference for urban design.

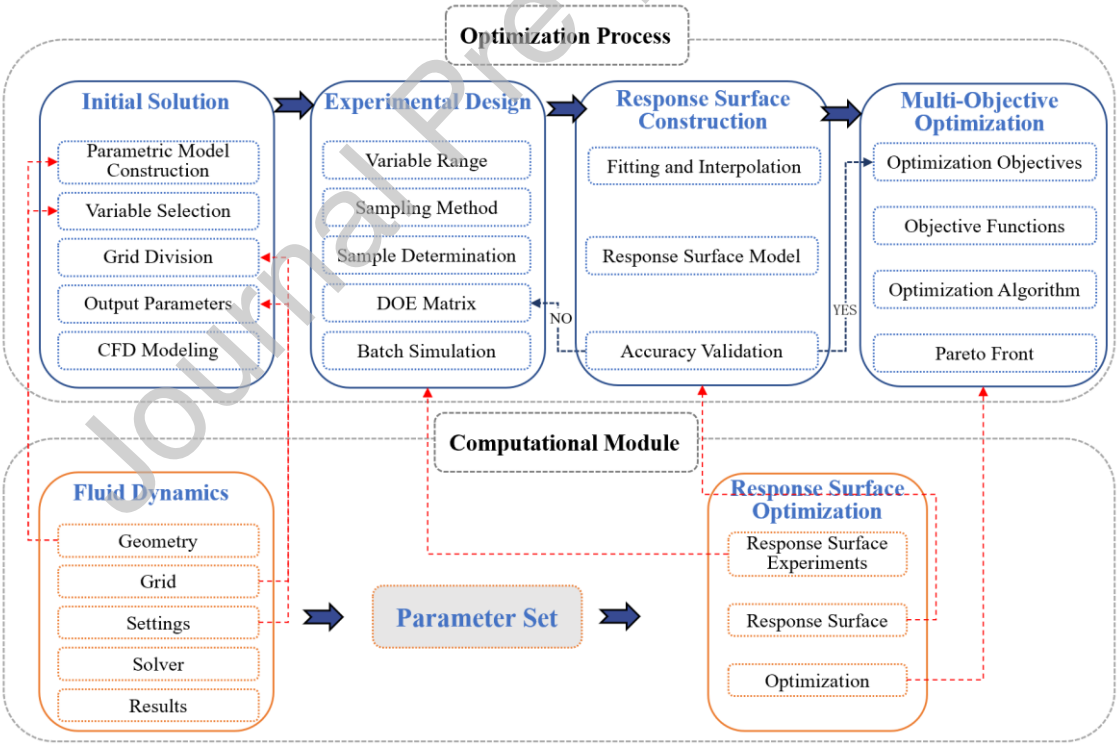

Fig. 1 Multi-objective optimization computational process based on numerical simulation and RSM

3.2. Performance Indicators

To comprehensively evaluate the dual environmental impacts of residential block morphology, this study employs two complementary performance indicators that quantify both human thermal comfort and air quality conditions.

3.2.1 Universal Thermal Climate Index (UTCI)

The Universal Thermal Climate Index (UTCI) serves as the primary indicator for assessing outdoor thermal comfort, representing the human physiological response to combined meteorological conditions. UTCI effectively quantifies the influence of climate parameter variations on outdoor thermal comfort through a sophisticated biometeorological model that considers the complex interactions between environmental factors and human thermoregulation. UTCI is determined using a sixth-order polynomial regression function that integrates four key meteorological parameters: air temperature, wind speed, mean radiant temperature, and relative humidity (expressed as water vapor partial pressure)[65].

$$UTCI = \text{offset}\left(T_a + T_{MRT} + U + P_{\text{vapor}}\right) + T_a \quad (1)$$

where, T_a represents air temperature, □; T_{MRT} is mean radiation temperature, □; U represents wind speed, m/s; P_{vapor} represents water vapor partial pressure, Pa.

The UTCI classification system provides clear thermal stress categories: values below 9°C indicate extreme cold stress, 9-26°C represents no thermal stress, 26-32°C indicates moderate heat stress, 32-38°C represents strong heat stress, 38-46°C indicates very strong heat stress, and values above 46°C represent extreme heat stress. For hot-humid climates like Shenzhen, the optimization target focuses on minimizing UTCI values to reduce heat stress during summer months.

3.2.2 Air Quality Index for $PM_{2.5}$ ($AQI_{PM2.5}$)

The Air Quality Index for $PM_{2.5}$ ($AQI_{PM2.5}$) serves as the air quality performance indicator, providing a standardized measure of fine particulate matter concentration levels and their potential health impacts. This index transforms raw $PM_{2.5}$ concentration data into a dimensionless scale that facilitates direct comparison across different urban morphological configurations. $AQI_{PM2.5}$ is calculated according to the provisions outlined in the Ambient Air Quality Standards [66], using a piecewise linear function that relates pollutant concentrations to health risk categories:

$$AQI_{PM2.5} = \frac{AQI_{Hi} - AQI_{Lo}}{BP_{Hi} - BP_{Lo}} (C_{PM2.5} - BP_{Lo}) + AQI_{Lo} \quad (2)$$

where, AQI_{Hi} and AQI_{Lo} are the upper and lower limit values of the AQI for $PM_{2.5}$; BP_{Hi} and BP_{Lo}

are the upper and lower limit value of the concentration range for $PM_{2.5}$; $C_{PM2.5}$ represents the concentration of $PM_{2.5}$.

The $AQI_{PM2.5}$ classification system defines air quality levels as follows: 0-50 indicates good air quality with minimal health impact, 51-100 represents moderate quality with acceptable conditions for most people, 101-150 indicates unhealthy conditions for sensitive groups, 151-200 represents unhealthy air quality for all individuals, 201-300 indicates very unhealthy conditions requiring health warnings, and values above 300 represent hazardous conditions. For urban planning applications, the optimization objective targets $AQI_{PM2.5}$ values below 100 to ensure acceptable air quality standards.

3.3. Parametric Model Development

3.3.1 Geometric Model and Typological Considerations

This study establishes a 6×6 building array surrounded by four main roads, forming an idealized urban residential block. While this regularized grid pattern represents a common typology in modern Chinese residential developments, it is important to acknowledge that different residential block typologies can impact environmental performance. Recent research has demonstrated that block configuration—including perimeter blocks, courtyard typologies, point towers, and slab arrangements—substantially influences solar radiation absorption, wind patterns, and resulting thermal conditions [67, 68]. The grid typology selected for this study represents a balance between computational feasibility and practical relevance. Grid patterns remain prevalent in rapid urbanization contexts due to their development efficiency and standardized planning approval processes [69]. Studies have shown that tall building blocks can improve outdoor thermal comfort through enhanced shading while potentially restricting ventilation [70], while their shape can influence air circulation and air quality in various part of the building and site [71]. A review of 258 studies (2011–2022) found that variations in urban morphology indicators—such as building density, street canyon aspect ratio, and sky view factor—affect solar radiation absorption, with certain configurations enhancing or reducing potential heat gain, thereby influencing outdoor thermal comfort [72].

The initial layout of the buildings, road lengths, and computational domain of this research is illustrated in Fig. 2. Key variables, including the length (L), width (W), height (H), the angle with the wind direction (A), transverse spacing (S), and longitudinal spacing (S') of the buildings, are

depicted in Fig. 2. While maintaining the grid typology constant, these parametric variations allow exploration of morphological optimization within this specific urban form. The optimization results should therefore be interpreted within the context of grid-pattern residential blocks, with different optimal parameters likely emerging for alternative typologies.

It is important to note that during the optimization process, changes in parameters may result in final morphology parameters differing from their initial definitions. To maintain consistency, the same naming convention is applied for changed parameters, supplemented by corresponding notations for distinction. The actual research area is the 4×4 buildings array inside Fig. 2, with the outermost buildings set to simulate the impact of surrounding buildings on the physical environment of the research area. Inside the research area, three measurement points are set near each external facade of the buildings at a height of 1.5 m, 3 m away from the buildings, and located at the 1/4, 1/2, and 3/4 positions of the facade, respectively, as shown in Fig. 2. These measurement points change with the variations in building length and width.

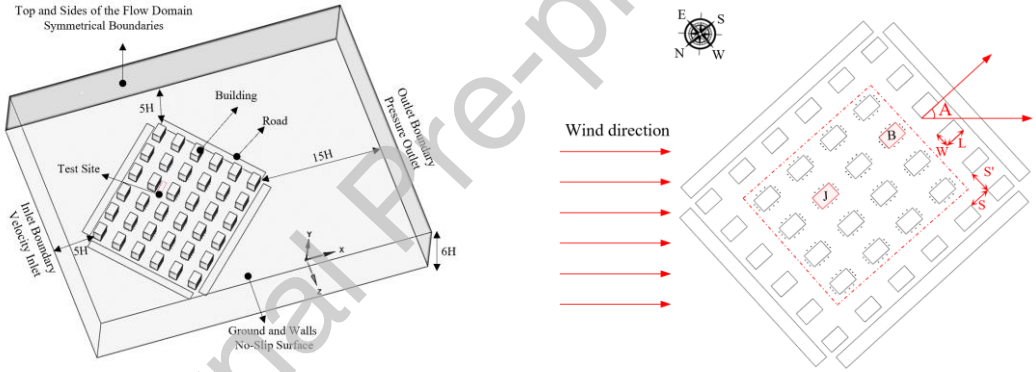

Fig. 2 Ideal residential block morphology layout and parameterized control variables

Referring to the regulations for buildings and roads in the "Shenzhen City Planning Standards and Guidelines" (2021 version) [73], the range of variation for the basic variables of the ideal residential block morphology is shown in Table 1. Since the floor area ratio (FAR) of residential land in Shenzhen is mostly in density zones two and three, the FAR is set between 3.0 and 6.0, with residential buildings being multi-story and high-rise. Roads are aligned with the buildings and are designed as six-lane dual carriageways, with each lane having a width of 3.25 m and the total road width being 19.5 m, and the buildings' setback is set to 9 m.

Table 1 Parameterized control variables and ranges

Buildings parameters	Range	Initial Value	Type of Variation
Length (L)	25 m ~ 70 m	26 m	Continuous
Width (W)	25 m ~ 70 m	48 m	Continuous

Height (H)	24 m ~ 100 m	62 m	Continuous
Angle with the wind direction (A)	-2.55° ~ 87.45°	42.45°	Continuous
Transverse Spacing (S)	24 m ~ 80 m	52 m	Continuous
Longitudinal Spacing (S')	24 m ~ 80 m	52 m	Continuous

The limitations of focusing on a single typology are acknowledged. Future research should extend this optimization framework to comparative analyses across different block typologies, as the interactive effects between thermal environment and air quality may manifest differently in perimeter, courtyard, or hybrid configurations. Nevertheless, the grid typology provides a valuable baseline for understanding morphological optimization principles that can inform broader urban design strategies.

3.3.2 Boundary Conditions and Input Parameters

When simulating the thermal environment of urban residential blocks, it is common to use meteorological parameters from a typical meteorological day in the local area as input to ensure broadly applicable results. However, identifying a "typical pollution day" involves more complexity. It depends on factors such as the dates when air quality exceeds standards for a sustained period, the influence of pollution sources, and specific meteorological conditions. Additionally, $PM_{2.5}$ concentrations are largely influenced by dispersion from the surrounding environment and emission sources. While closely tied to meteorological factors, $PM_{2.5}$ exhibits strong randomness and regional variability, making it unsuitable to describe using the concept of a "typical day" as applied to meteorological parameters. To address this, this study compiled meteorological parameters and $PM_{2.5}$ concentrations in Shenzhen over the past five years (2018–2022). Analysis revealed that September had the highest number of pollution days, with a total of 39 days—far exceeding other months. Thus, the average $PM_{2.5}$ concentration and meteorological parameters at noon in September were selected as input parameters. Since the recorded pollution days in the study were not rainy days, the compiled input parameters exclude rainy days. These parameters are detailed in Table 2.

The emission rate of fine particulate matter from roads is calculated based on the methods described in “Technical Guidelines for the Compilation of Road Mobile Source Emission Inventories”, and the number of vehicles and their driving conditions, vehicles/1000m (https://opendata.sz.gov.cn). The total emission rate of $PM_{2.5}$ concentration from roads varies with the length of the road and is modeled mathematically within the parametric model.

Table 2 Inlet parameters of CFD model

Parameter	Value
Air temperature	29.97 (°C)
Radial wind speed (10m)	-1.17 (m/s)
Zonal wind speed (10m)	-1.07 (m/s)
Direct radiation	545.40 (W/m^2)
Diffuse radiation	123.34 (W/m^2)
Effective sky temperature	15.79 (°C)
$PM_{2.5}$ Concentration at Inlet	35.78 (ug/m^3)

3.3.3 Two-way Coupled Numerical Simulation

The computational logic of the two-way coupled numerical model for the outdoor thermal environment and $PM_{2.5}$ has been developed by the authors in previous research [55], and its workflow has been illustrated in Fig. 3. Input parameters include ambient conditions, material properties, and geometric factors. The two-way coupling model employs steady-state three-dimensional Reynolds-Averaged Navier-Stokes equations for incompressible turbulence, incorporating the Boussinesq approximation. Energy coupling is achieved through the Discrete Ordinates model, with atmospheric absorption and scattering coefficients dynamically adjusted based on $PM_{2.5}$ concentrations and incorporated into the iterative calculation process. This process is implemented through a user-defined function, and the file is read when the Discrete Ordinates model is called. Momentum coupling is implemented using the Discrete Phase Model, which accounts for forces such as gravity, fluid drag, Saffman lift, pressure gradient, and thermophoretic force, all based on velocity terms. The numerical discretization method uses the finite volume method, and the upwind second-order format is adopted; the pressure-based coupled algorithm is used to solve the equations. The residual convergence standard is set to 10E-6, and the calculation parameters of the measurement points are monitored to ensure that they reach a stable state. The complete governing equations, boundary conditions, and numerical solution methodology are provided in Appendix A.3, with comprehensive model validation presented in Appendix A.4.

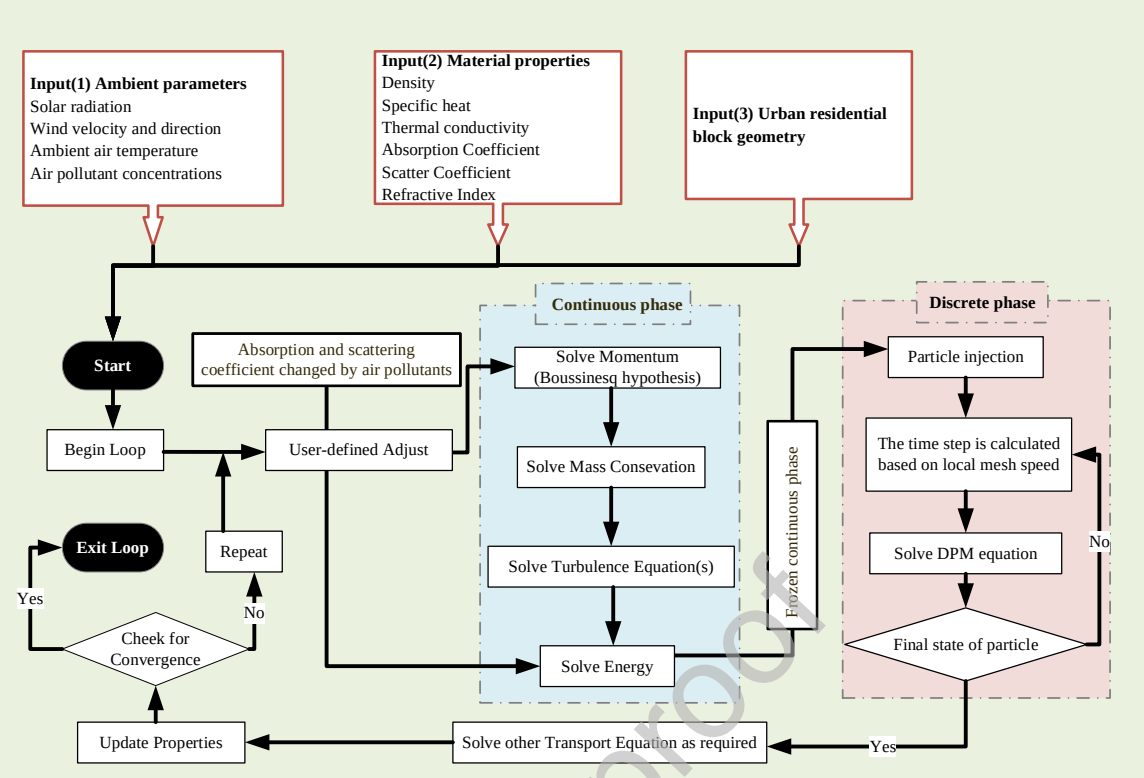

Fig. 3 Two-way coupled numerical simulation between outdoor thermal environment and $PM_{2.5}$ in residential blocks

3.4. Response Surface Model Development

The selection of an appropriate surrogate modeling technique is critical for achieving accurate predictions while maintaining computational efficiency. Several methods were considered for constructing the response surface model, including polynomial regression, kriging (Gaussian process regression), radial basis functions (RBF), and non-parametric regression. Table 3 provides a comparative analysis of these approaches.

Table 3 Comparison of surrogate modeling methods for urban environmental optimization

Method	Advantages	Limitations	Suitability
Polynomial Regression	Simple implementation; Fast evaluation; Clear mathematical form	Poor for highly nonlinear relationships; Requires predetermined order; Prone to overfitting with high dimensions	Limited - Urban environmental relationships are highly nonlinear
Kriging/Gaussian Process	Provides uncertainty estimates; Excellent for smooth functions; Optimal interpolation	Computationally expensive for large datasets; Assumes stationarity; Struggles with discontinuities	Moderate - Good accuracy but computational cost can be prohibitive
Radial Basis	Flexible for complex	Can become ill-	Moderate - Good flexibility

Functions	shapes; Good for scattered data; No need for structured grid	conditioned; Requires careful selection of basis centers; No uncertainty quantification	but stability concerns
Non-Parametric Regression	No assumptions about data distribution; Captures complex interactions; Robust to outliers; Adaptive to local features	Less interpretable; Can overfit without proper regularization	High - Best suited for complex urban phenomena with unknown relationships

In this research, the DOE is structured to efficiently and comprehensively capture the key morphology characteristics of residential block configurations by simulating diverse combinations of input parameters with a limited number of samples. Experimental evaluation metrics are referred to as output variables, while factors potentially influencing these metrics are termed input variables. The discrete or continuous states of these influencing factors are designated as levels. For parametric analyses, the input variables vary continuously, as summarized in Table 1. To ensure a uniform and representative distribution of sample points across the entire design space, this study employs the Latin Hypercube Sampling technique. This method systematically distributes sample points to evenly cover the parameter space, even with a constrained number of samples. The ranges and types of variation for morphology variables are detailed in Table 1. A total of 200 sample points is generated. These samples are subsequently analyzed using RSM to explore and quantify the relationships between input variables and output variables.

The Non-Parametric Regression method was selected for this study based on several key advantages particularly relevant to urban environmental modeling. First, it does not rely on specific assumptions about data distribution or functional form, allowing the data to reveal the complex, potentially discontinuous relationships between morphological parameters and environmental outcomes [74]. This is crucial given the nonlinear interactions between building geometry, thermal environment, and pollutant dispersion that may include threshold effects and local phenomena. Secondly, non-parametric methods excel at capturing local features and interactions that parametric models might smooth over [75]. Urban microclimates often exhibit localized effects where small changes in morphology can cause disproportionate environmental responses—phenomena that global parametric models struggle to represent. The method's adaptive bandwidth selection automatically adjusts model complexity based on local data density,

providing more flexibility in regions with rapid changes while maintaining stability in smoother regions. Thirdly, the method demonstrates superior performance with the moderate sample size (200 points) generated through Latin Hypercube Sampling. While kriging might provide slightly better interpolation accuracy in smooth regions, its computational requirements scale poorly with sample size ($O(n^3)$ for matrix inversion), making it impractical for iterative optimization. Non-parametric regression achieves comparable accuracy with better computational efficiency, fit for the thousands of evaluations required during genetic algorithm optimization. The specific implementation employs locally weighted scatterplot smoothing (LOESS) with automatic bandwidth selection through cross-validation.

To validate this methodological choice, preliminary tests compared polynomial regression (third-order), kriging, and non-parametric regression on a subset of 50 samples. Non-parametric regression in this study achieved the lowest cross-validation error (RMSE = 0.42°C for UTCI, 1.23 for $AQI_{PM2.5}$) compared to polynomial regression (RMSE = 0.89°C, 2.67) and kriging (RMSE = 0.51°C, 1.45), while requiring 73% less computational time than kriging for model construction. The DOE sample points are divided into two sets: 80% (160 samples) for the training dataset and 20% (40 samples) for the validation dataset. Both datasets are designed to maintain as uniform a distribution of the design variables as possible. After removing outliers, the training dataset contains 153 samples, while the validation dataset includes 36 samples. More detailed discussions on the non-parametric regression based RSM validation and analysis will be included in the Results chapter.

3.5. Multi-objective Optimization

3.5.1 Optimization Problem Formulation

In the process of optimizing the morphology of urban residential block, the results do not manifest as a single, absolute optimal solution. Instead, they form a set of relatively optimal solutions that balance the two design objectives: UTCI and $AQI_{PM2.5}$. As indicated by the RSM analysis, UTCI and $AQI_{PM2.5}$ exhibit differing trends with variations in the input parameters. This study employs a multi-objective optimization approach aimed at minimizing both UTCI and

$AQI_{PM2.5}$. When it is not feasible to achieve optimality for all objectives simultaneously, a balanced set of solutions is obtained. The mathematical model for multi-objective optimization is presented as follows:

$$\min_{x \in E} \quad : f_j(x) = \left(f_1(x), f_2(x)\right) \tag{3}$$

$$x = (x_1, x_2, x_3, x_4, x_5, x_6) \tag{4}$$

$$E = \{x | x_i' \leq x_i \leq x_i'',\ i = 1, 2, \cdots, 6\} \tag{5}$$

where, x is design variables, consisting of the six morphology parameter variables listed in Table 1; $f_j(x)$ is the j objective function of the model; E is the boundary constraints for the set of morphology parameter variables. x_i' and x_i'' are lower and upper boundary of the value range for the design variable.

In the multi-objective optimization experiments, morphology parameter constraints were further considered to ensure the practical applicability of the optimization results and compliance with the Shenzhen Urban Planning Standards and Guidelines (2021) [73]. Four additional variables were introduced during the optimization phase: FAR, spacing ratios (SR), and coverage ratio (CF). The value ranges for these variables were determined with reference to [73]. The range of R being 6.0 and 3.0 has the most extensive distribution in Shenzhen. Thus, the buildings were designed as multi-story or high-rise structures. The height range was set between 24 m and 99 m, with a fixed floor height of 3 m per story. The upper limits for SR and CF were set to 0.6 and 0.25, respectively.

The guidelines in [73] recommend that for buildings taller than 60 m, the maximum building width should not exceed 60 m. Additionally, the minimum transverse and longitudinal spacing for high-rise residential buildings should be no less than 24 m and 18 m, respectively. In this study, the building length and width are allowed to vary freely during optimization, but the minimum spacing between buildings is uniformly set to 24 m. Although the guidelines do not specify a maximum spacing, this study sets the maximum buildings spacing to 80 m. Furthermore, the angle between buildings and the dominant summer wind direction is required to be less than 30°. To achieve this, the orientation of buildings was adjusted by rotating them clockwise and counterclockwise by 45° from their original alignment, resulting in an angle range of -2° to 87°. The step size for this variable was set to 1°. The value ranges, step sizes, and relationships for the design variables are detailed in Table 4.

Table 4 Characteristics of design variables

Type	Design Variables	Value Range	Step Size	Parameter Relationship
Design Variables	L	25 m ~ 60 m	1 m	
	W	25 m ~ 60 m	1 m	
	A	- 2.55°~87.45°	1°	—
	S'	24 m~80m	1 m	—
	S	24 m~80m	1 m	—
Constraints	FAR	3~6	Continuous	(L*W*36*H/3)/(L*6+S*5+18)/(W*6+ S'*5+18)
	J_1	≤0.6	Continuous	(L*6)/(L*6+S*5+18)
	J_2	≤0.6	Continuous	(W*6)/(W*6+ S'*5+18)
	F	≤0.25	Continuous	(L*W*36)/(L*6+S*5+18)/(W*6+ S'*5+18)

3.5.2 Optimization Algorithm

The study employed the Multi-Objective Genetic Algorithm (MOGA), which integrates population evolution strategies and a non-dominated solution screening mechanism. This approach facilitates a comprehensive exploration of the solution space, identifies a richer set of solutions, and avoids the pitfalls of local optima, making it particularly suitable for the optimization requirements of this research. In addition, three convergence criteria were established: maximum of 500 iterations, convergence threshold of 0.01, and maximum Pareto percentage of 80%. The parameters related to the MOGA are summarized in Table 5.

Table 5 Parameter settings for multi-objective optimization calculations

Category	Parameter	Minimum Value	Maximum Value	Objective	Weight
Attribute	UTCI	30	40	Minimize	0.5
	$AQI_{PM2.5}$	0	30	Minimize	0.5
Algorithm	MOGA	Initial Population 2000	Per Population 2000	Convergence Stability 1%	Maximum Iterations 500
		Pareto Ranking 1-5	Crossover Rate 0.9	Mutation Rate 0.01	Pareto Percentage

Initially, the multi-objective optimization module received morphology parameters. The genetic algorithm autonomously generated 2,000 initial samples, which were subsequently passed to the RSM. The model rapidly computed the output parameters, and the results were fed back into the genetic algorithm. Through selection, crossover, and mutation operations, a new generation of 2,000 samples was created, with input parameters forwarded again to the RSM. The algorithm

evaluated the convergence conditions to determine whether the optimization should terminate. If the criteria were satisfied, the optimization process concluded, and results were output; otherwise, iterations continued until the objectives were met.

3.5.3 Sensitivity Analysis

To examine the impact of simultaneous changes in multiple input parameters on model outputs and determine the sensitivity of each parameter in the Pareto front solution set, this study utilizes the Parameter Correlation module in ANSYS Workbench. The Spearman rank correlation coefficient is employed to quantify parameter sensitivity, ranging from [-1, 1], where the sign indicates positive or negative correlation. The calculation method is as follows:

$$r = \frac{\sum_i^n (X_i - \bar{X})(Y_i - \bar{Y})}{\sqrt{\sum_i^n (X_i - \bar{X})^2} \sqrt{\sum_i^n (Y_i - \bar{Y})^2}} \quad (6)$$

where, X_i represents the rank value of the design variable X in i sample; Y_i represents the rank value of the optimization objective Y in the i sample; n represents the total number of samples; $\bar{X}$ and $\bar{Y}$ represent the average rank value of the design variables and optimization objectives.

3.6 Case Study

The residential block analyzed in this study is located in Bao'an District, Shenzhen. As shown in Fig. 4, the renewal area is divided into three zones by newly constructed residential communities and public buildings. The morphology parameters of the Pareto frontier solutions are combined with the requirements outlined in the Shenzhen Urban Planning Standards and Guidelines [73] regarding floor area ratio (FAR), building density, and setback distances. According to the guidelines, secondary roads should have a width of 12m to 20m, and residential buildings adjacent to streets must maintain a minimum setback of 9m. When the layouts of buildings on adjacent zones are parallel or form an angle of less than 30°, and at least one of the buildings is residential, the minimum setback distance from the plot boundary must not be less than 12m. This residential block is classified under Density Zone 2 in Shenzhen, where the maximum FAR is 6, and the building density is capped at 25%. In optimization scheme, the angle between the building layout and the prevailing wind direction is constrained to 0°-15°, with all parameters determined based on the ratio values of the Pareto frontier solutions. The buildings are adjusted to maintain a length-to-width ratio within the range of 1.04 to 1.43. The block

morphology parameters corresponding to the optimized design scheme are listed in Table 6. The computational domain configuration, mesh generation procedures, and material properties are detailed in Appendix A.1 and A.2.

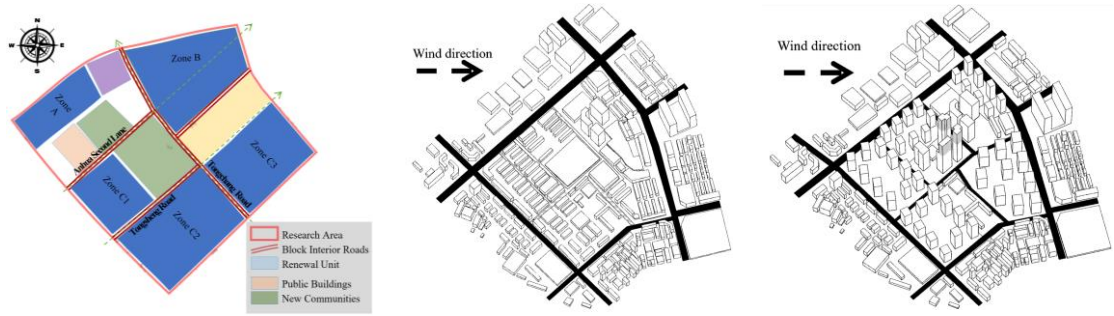

(a) Subdivision of construction land

(b) Layout of original block

(c) Layout of optimized block

Fig. 4 Research area land use division and geometric models

Table 6 Residential block morphological schemes

Building parameters	A	B	C1	C2	C3
Length (m)	24	35	32	27	31
Width (m)	22	30	24	23	26
Length/Width Ratio	1.09	1.17	1.33	1.17	1.19
Lateral Spacing (m)	38	42.5	43	44	58
Longitudinal Spacing (m)	28.5	23	26	25	46
Height (m)	60;81	66	66, 72	69, 75	54, 82
Lateral Spacing/Height Ratio	1.58	1.55	1.53	1.57	1.59
Density	0.25	0.25	0.25	0.25	0.25

The measured inlet parameters for numerical simulation at the research area's observation sites from 2021 to 2023 were statistically analyzed. Parameters measured at 2:00 pm in September over the past two years were selected, as this time period features high temperatures and elevated $PM_{2.5}$ concentrations. In addition, the inlet parameters represent the average values recorded under sunny or partly cloudy-to-sunny conditions. The prevailing wind direction was determined based on 16-direction wind statistics, identified as southerly, with an average wind speed of 1.03 m/s. To ensure effective simulation of air pollution, days with pollution under southerly wind conditions were selected, where the average $PM_{2.5}$ concentration was 37.01 ug/m^3. Solar radiation intensity parameters were obtained from the Xihe Energy Big Data Platform (https://xihe-energy.com/). The direct and diffuse solar radiation intensities recorded at the specified time over the past two years under sunny or partly cloudy-to-sunny conditions were averaged, and the results are listed in Table 7.

Table 7 Inlet parameter for numerical simulation in target area

Parameters	Values	Notes
Wind Speed (m/s)	1.03	Average Wind Speed under Prevailing Wind Direction
Wind Direction	Southerly wind	Prevailing wind direction
Air Temperature (□)	32.16	
$PM_{2.5}$ Concentration (ug/m^3)	37.01	
Direct Solar Radiation Intensity (W/m^2)	435.67	
Diffuse Solar Radiation Intensity (W/m^2)	291.10	

To accommodate the complex geometry of the building clusters, utilized a tetrahedral mesh. The grid size at the domain inlet was set to 3 m, while surface meshes for buildings, roads, and the ground were assigned a size of 5 m. The boundary surface meshes of the domain were set to 10 m, and the maximum cell size within the domain was limited to 15 m, with a growth rate of 1.1. The boundary layer mesh had an initial size of 0.1 m, also with a growth rate of 1.1. The two-way coupled model between thermal environment and $PM_{2.5}$ as shown in Fig. 4 is used. The model validation demonstrates good agreement with field measurements as detailed in Appendix A.4, with temperature predictions achieving MAE of 1.03°C and PM□.□ concentration predictions showing relative errors below 20%.

4 Results

4.1. Response Surface Model Validation and Analysis

Prior to employing the response surface model for optimization, its predictive accuracy should be evaluated against CFD simulation results to ensure reliable performance across the design space. The maximum absolute errors of the RSM for the $AQI_{PM2.5}$ and UTCI validation points are found to be 8.13% and 5.37%, respectively, while the coefficients of determination (R^2) for the training data are 0.98 and 0.99. The results demonstrate good predictive performance, both locally and globally. Detailed statistical performance metrics and validation procedures are described in Appendix A.6.

Fig. 5 illustrate the predicted versus actual values for the validation dataset, showing controlled deviations, further validating the model's accuracy. Given its strong predictive performance, the RSM is considered a reliable substitute for computationally intensive CFD numerical simulations during the optimization phase, offering significant reductions in computational time without compromising the quality of the results.

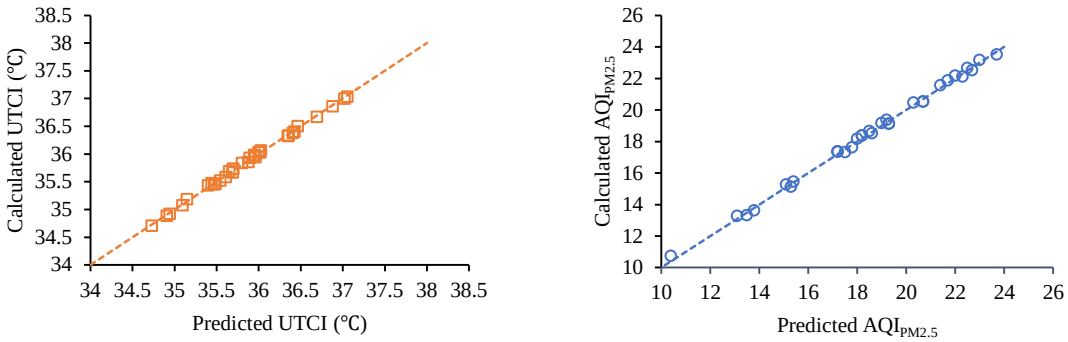

（a） UTCI （b） AQI$_{PM2.5}$

Fig. 5 Accuracy verification of RSM

As shown in Fig. 6(a), when the building length (L) is 70 m and the transverse spacing (S) is approximately 25 m or 60 m, the UTCI values are lower. Conversely, when both the length and transverse spacing are large, the outdoor UTCI reaches its maximum value of 36.80 □. In Fig. 6(b), the lowest UTCI value of 35.61 °C occurs when the building width (W) is 70 m and the longitudinal spacing (S') is 20 m. In contrast, when the width is 24 m, variations in longitudinal spacing have negligible effects on UTCI. This suggests that, in architectural optimization, width should take precedence over longitudinal spacing. The relationship between the angle of building and wind direction (A), height (H), and UTCI is depicted in Fig. 6(c).

To quantify the relative importance of these parameters, we conducted a comprehensive sensitivity analysis using the Spearman rank correlation coefficient (detailed in Section 4.3. Sensitivity Analysis Results). The analysis reveals that among the morphology parameters, building longitudinal spacing (S') has the most significant impact on UTCI with a correlation coefficient of -0.81, followed by building height (H) at -0.73, and building width (W) at -0.63. The angle between building and wind direction (A), while showing strong effects in the response surface visualization, demonstrates a relatively lower sensitivity (±0.18) within the Pareto front solution set due to the constrained angle range in optimal solutions. Specifically, when the angle is approximately -2.55° or 87.5°, the outdoor UTCI is minimized at 34.12°C. Conversely, within the range of 20° to 40°, UTCI values remain consistently high regardless of height. These quantitative findings, derived from sensitivity analysis of Pareto-optimal solutions (Section 4.2), highlight that the optimal configuration for a single parameter may not necessarily correspond to the most effective strategy for improving the thermal environment.

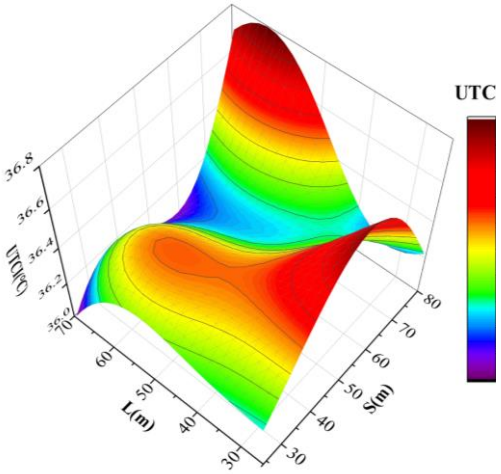

(a) building length (L) and transverse spacing (S)

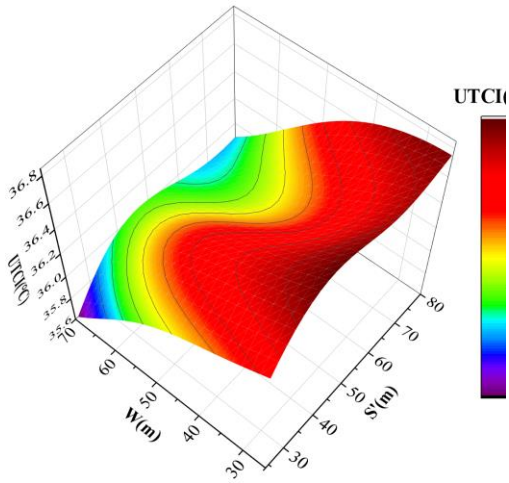

(b) building width (W) and longitudinal spacing (S')

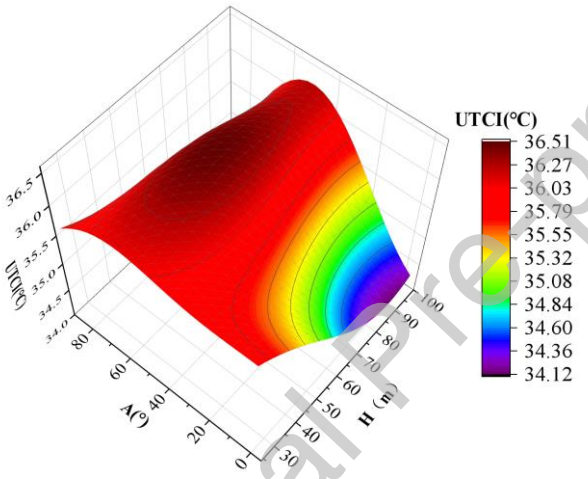

(c) building angle (A) and height (H)

Fig. 6 RSM of morphology parameters for residential blocks and UTCI

Fig. 7(a) illustrated the relationship between building length (L) and transverse spacing (S) with $AQI_{PM2.5}$. When length and transverse spacing are relatively small, $AQI_{PM2.5}$ values are highest. Conversely, when the transverse spacing is approximately 75 m, $AQI_{PM2.5}$ values tend to be low. Notably, even if the length increases to 70 m, $AQI_{PM2.5}$ remains high when the transverse spacing is limited. This highlights the significant influence of transverse spacing on $AQI_{PM2.5}$. Fig. 7(b) further demonstrates that smaller building widths (W) and longitudinal spacings (S') result in higher $AQI_{PM2.5}$ values, reinforcing the observation that dense buildings layout hinder the dispersion of $PM_{2.5}$. When the building width and longitudinal spacing are around 70 m and 55 m, respectively, $AQI_{PM2.5}$ values also appear elevated. In contrast, $AQI_{PM2.5}$ values are generally lower when the longitudinal spacing is approximately 80 m. The effects of the angle of building and

wind direction (A) and height (H) on $AQI_{PM2.5}$ are shown in Fig. 7(c). $AQI_{PM2.5}$ reaches its maximum value when both angle and height are at maximum. However, when the height is 24 m, $AQI_{PM2.5}$ values remain low regardless of changes in the angle. Interestingly, when the buildings align more closely with the wind direction, air pollution in the target area is exacerbated.

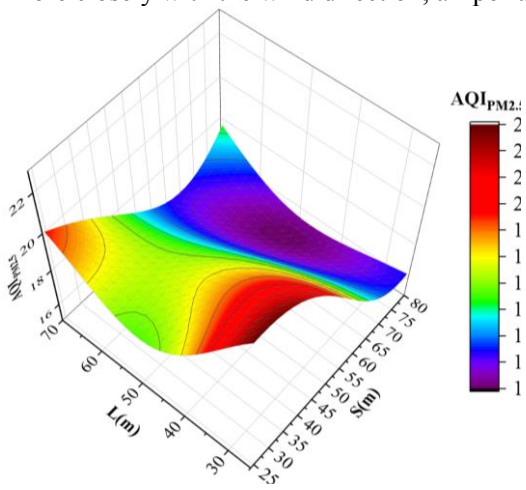

(a) building length (L) and transverse spacing (S)

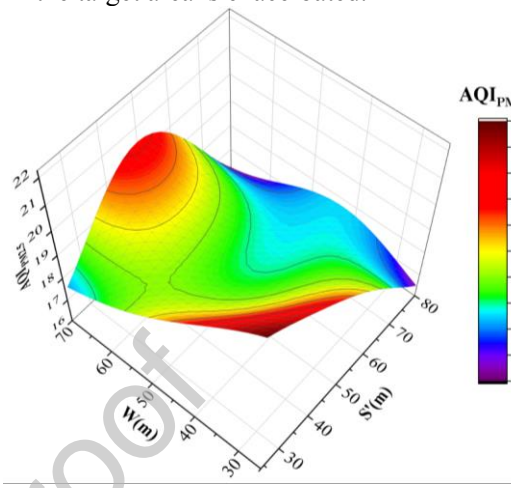

(b) building width (W) and longitudinal spacing (S')

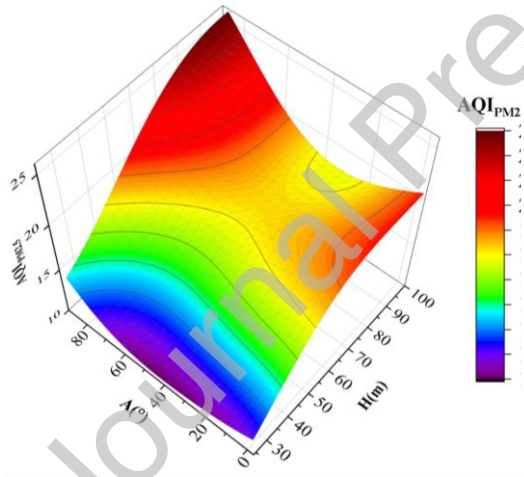

(c) building angle (A) and height (H)

Fig. 7 RSM of morphology parameters for residential blocks and $AQI_{PM2.5}$

4.2. Optimization Results and Pareto Front

Following the validation of the response surface model, multi-objective genetic algorithm optimization was performed to identify morphological configurations that balance thermal comfort and air quality objectives. As illustrated in Fig. 8, convergence was achieved after 21 iterations for the MOGA optimization, with 80% of the solutions forming the Pareto front. The convergence

stability reached 0.91, indicating robust performance.

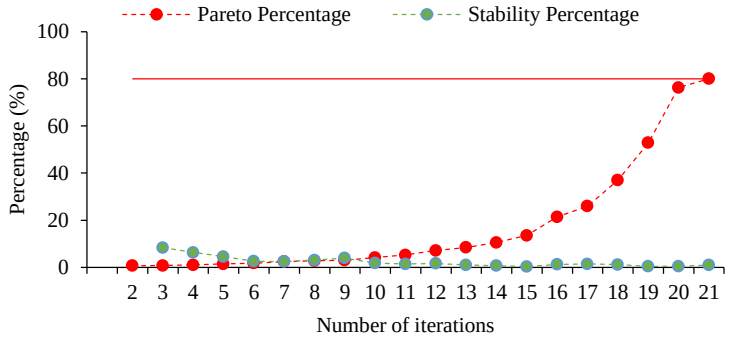

Fig. 8 The iterative convergence process of multi-objective optimization

To optimize the thermal environment and $PM_{2.5}$ levels in an ideal residential block, the distribution of the Pareto solution set is illustrated in Fig. 9. The solution set is categorized into five levels: red points indicate Pareto front solutions, representing non-dominated options, while the remaining-colored points signify dominated solutions. A clear trade-off emerges between UTCI and $AQI_{PM2.5}$, where a decrease in UTCI corresponds to an increase in $AQI_{PM2.5}$. The $AQI_{PM2.5}$ values within the Pareto set are notably low, ranging from 9.91 to 20.04, indicating high air quality. Conversely, the UTCI values are relatively high, between 34.32 □ and 36.31 □, with minimal variation, yet still indicating conditions of overheating. Given that outdoor overheating is a major environmental challenge during Shenzhen's summer, and the air quality in the Pareto set remains excellent, candidate solutions with lower UTCI should be prioritized.

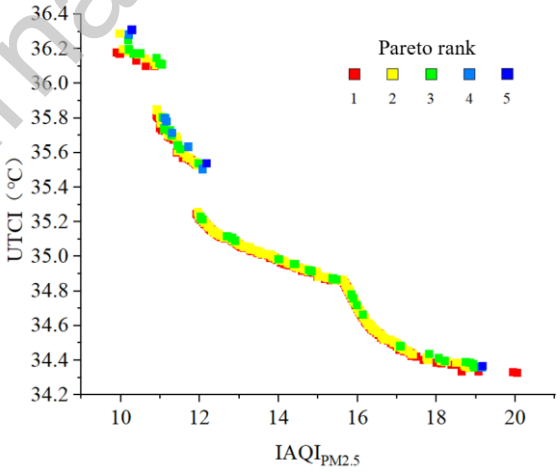

Fig. 9 Dominated and non-dominated solutions of UTCI and $AQI_{PM2.5}$

In Fig. 10, the distribution of morphology parameters within the Pareto front solution set is presented. The dual objectives of UTCI and $AQI_{PM2.5}$ were considered, with constraints applied to the FAR, interspace rate, and density according to relevant specifications. As a result, the range of

the Pareto front solution set from the multi-objective optimization differs from the optimal results derived via the RSM. The building length (L) exhibits a distinct three-stage interval distribution, with corresponding UTCI and $AQI_{PM2.5}$ values aligned with the intervals listed in Table 8. Similarly, the building transverse spacing (S) also follows a clear interval distribution, forming a corresponding relationship with the building length intervals. To further analyze the interaction between design variables and objective functions and identify the optimal combination of morphology parameters, an interval analysis is conducted on the Pareto rank 1 solution set.

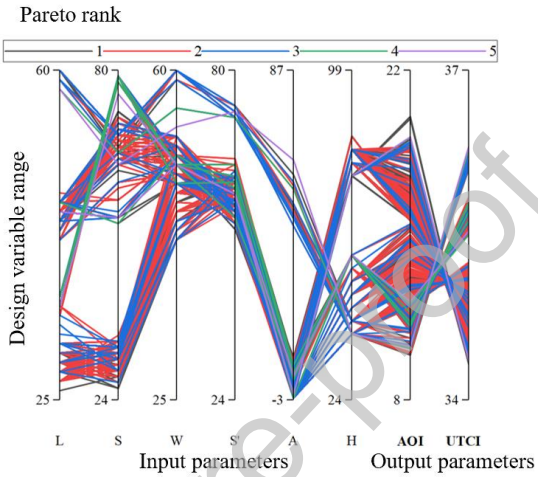

Fig. 10 Parameter intervals corresponding to the pareto front solution

The building length (L) can be divided into three distinct intervals: 26 m to 36 m, 42 m to 46 m, and 60 m, with the corresponding parameter ranges detailed in Table 8. Among these, the UTCI value is highest when the building length is 60 m. However, this interval contains only 10 sample points, notably fewer than the other intervals, and is therefore excluded from further discussion. For intervals 1 and 2, the FAR range from 3.00 to 4.08 and 5.11 to 6.00, respectively, representing the lower and upper limits of the design variable range. The corresponding building heights (H) are 39 m to 57 m for the first interval and 75 m to 84 m for the second. The angle range between the building and the wind direction is generally consistent, falling within -2° to 9°. Therefore, when optimizing building morphology, the appropriate length and FAR can be selected based on specific FAR requirements.

Table 8 Statistical analysis of parameter intervals for Pareto front

Design Variables	Value Range 1	Value Range 2	Value Range 3
L	26 m~36 m	42 m~52 m	60 m
S	26 m~34 m	54 m~73 m	66 m~69 m
W	42 m~52 m	48 m~53 m	59 m~60 m
S'	55 m~64m	53 m~59 m	72 m~74 m

A	-2°~8°	-2°~9°	-47°~59°
H	39 m~57m	75 m~84 m	39 m~42m
AFR	3.00~4.08	5.11~6.00	3.16~3.47
SR_1	0.28~0.43	0.33~0.41	0.41~0.42
SR_2	0.35~0.45	0.39~0.43	0.39~0.40
CF	15.79%~24.96%	20.22%~23.99%	23.96%~24.80%
UTCI	34.86~35.83	34.32~34.86	36.10~36.17
$AQI_{PM2.5}$	10.91~15.32	15.62~20.04	9.91~10.86

In the Pareto front solution set, where equal target weights were applied, three non-dominated solutions were selected, demonstrating advantages over other alternatives. As shown in Table 9, the optimal solution, alternative C, adheres to restrictions on FAR, interspace rate, and density. Through optimization algorithm screening, the building length (L) and width (W) were determined to be 45 m and 52 m, respectively. The RSM results indicate that a lower UTCI correlates with larger bulding dimensions. Additionally, the transverse spacing (S) of alternative C is 67 m, closely matching the 68.14 m spacing associated with the lowest UTCI in the RSM. The building length axis aligns parallel to the wind direction, consistent with RSM. The building heights (H) in the three candidate schemes are 39 m, 48 m, and 81 m, respectively. Using the geometric parameters of the optimal solution C, a new geometric model was created in ANSYS Workbench. Based on the parameter settings in Section 5.2, CFD simulations were conducted. The calculated UTCI and $AQI_{PM2.5}$ values were 34.52 □ and 16.67, respectively, compared to the optimal solution C's values of 34.31 □ and 16.19, resulting in relative errors of 0.61% and 2.96%. This confirms that the method can effectively replace bidirectional coupling model calculations, providing accurate predictions of the thermal environment and air quality within the ideal residential block.

Table 9 Alternative optimization schemes

Design Variables	A	B	C
L (m)	29	31	45
S (m)	33	31	67
W (m)	49	48	52
S' (m)	60	61	56
A (°)	-2	-2	1
H (m)	39	48	81
UTCI（□）	35.15	35.01	34.52
$AQI_{PM2.5}$	12.31	13.75	16.67

4.3. Sensitivity Analysis Results

To understand the relative importance of morphological parameters and guide practical

design decisions, a sensitivity analysis was conducted on the Pareto-optimal solutions. Fig. 11 illustrates the local sensitivity of UTCI and $AQI_{PM2.5}$ to the morphology parameters of the residential block. The parameters exhibit opposite effects on UTCI and $AQI_{PM2.5}$. Among them, the building longitudinal spacing (S') has the most significant impact, with a sensitivity indicator of ±0.81, whereas the transverse spacing (S) shows negligible influence on the physical environment. This indicates that ventilation channels aligned with the wind direction have a considerable effect on the environment and should be prioritized during block morphology optimization. Conversely, ventilation channels perpendicular to the wind direction can be adjusted flexibly based on practical needs. The building height (H) also plays an important role, with a sensitivity indicator of ±0.73. Increasing building height improves shading, thereby reducing the thermal environment index (UTCI). However, taller buildings enhance wind resistance, potentially degrading outdoor air quality, necessitating careful monitoring of its overall impact. The building width (W) shows a sensitivity of ±0.63, exerting a greater influence on the physical environment than the length (L). Additionally, while the rotation angle (A) of the buildings has the greatest effect in the RSM, its impact within the Pareto front solution set is minimal (±0.18) due to the narrow range of angle values, which limits its influence on the physical environment.

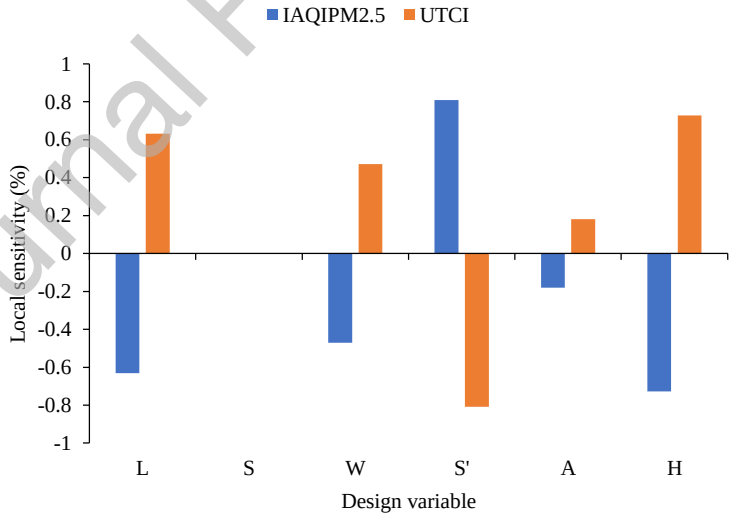

Fig. 11 Sensitivity indicators of physical environment to morphology parameters

When optimizing the physical environment of urban residential block, it is crucial to balance the positive and negative impacts of various parameters. The sensitivity ranking of morphology parameters with respect to UTCI and $AQI_{PM2.5}$ is as follows: building longitudinal spacing (S'), height (H), length (L), width (W), building rotation angle (A), and transverse spacing (S). During

optimization, parameters with low sensitivity can be adjusted more flexibly based on design requirements and the specific conditions of the site, while parameters with high sensitivity should be kept within their optimal range as much as possible.

4.4. Optimization Strategy

4.4.1 Building Orientation Guidelines

Based on the optimization results and sensitivity analysis, practical design strategies are developed to guide morphological decisions for different urban development contexts in this study. Building orientation emerged as a critical factor influencing both thermal and air quality performance, though its optimal configuration depends on local pollution sources and prevailing wind patterns. In the RSM, the variation of the building rotation angle has the greatest impact on UTCI, $AQI_{PM2.5}$, and wind speed. The worst thermal environment quality occurs when the angle is 53.64°, while the best outdoor air quality is at an angle of 46.18°. This phenomenon is attributed to the consideration of $PM_{2.5}$ at the inlet of the catchment area as the main pollution source in the multi-objective optimization calculation. When the wind direction is almost parallel to the building longitudinal passage, the ventilation effect is optimal, effectively carrying away the building's residual heat, but at the same time, it may also introduce more fine particulate matter. Therefore, when determining the orientation of a group of buildings, it is also necessary to clearly understand the pollution source situation in the study area.

The "Shenzhen City Planning Standards and Guidelines" (2021) [73] require consideration of the prevailing wind direction's impact on buildings layout. In the "Standard for Energy-efficient Design of Residential Buildings in Hot Summer and Warm Winter Regions" (JGJ75-2012), it is also emphasized that when designing a group of buildings, natural ventilation should be considered, and the layout of buildings should preferably be north-south or close to the north-south direction. In the Pareto front solution, the angle between the building orientation and the wind direction is -2° to 9°, where the incoming wind direction is basically parallel to the axis of the building width direction. However, in actual research, due to the influence of the surrounding area on the wind environment of the block, it may not be possible to simultaneously meet the requirements of the prevailing wind direction and sunlight, or the direction of the plot and streets may not meet the requirements for the north-south arrangement of buildings. In this case, try to

control the angle between the building width and the prevailing wind within 15° to promote ventilation within the block.

4.4.2 Spacing and Height Optimization

The interplay between building spacing and height represents the most influential morphological relationship, requiring careful balance to achieve environmental objectives while meeting density requirements. The RSM results show that a larger building height corresponds to lower UTCI and $AQI_{PM2.5}$ values. At the same time, the larger the building spacing, the smaller the corresponding UTCI value. For example, in the non-dominated solution C, the transverse spacing and perpendicular building spacing are 56 m and 67 m, respectively. Due to the restrictions of the FAR, they did not reach the upper limit of the optimization range of 80 m. Building design and urban planning design codes often only stipulate the minimum spacing of buildings.

The sensitivity ranking of morphology parameters indicates that the impact of building transverse spacing and height on UTCI and $AQI_{PM2.5}$ is the greatest. Therefore, when optimizing the morphology design of residential block, these two parameters should be reasonably designed. In the Pareto front solution set, when the FAR is close to 3, the transverse spacing is 55 m to 64 m, and the building height is 39 m to 57 m; when the FAR is close to 6, the transverse spacing is 53 m to 59 m, and the building height is 75 m to 84 m.

However, in actual building design and urban planning design, not only the building spacing and height need to be considered, but also the optimization of the plot's form, FAR, building density, and other restrictions. It is not possible to optimize the design according to the interval values of the Pareto solution set in all study areas in Shenzhen. The specific parameters of building transverse spacing (S) and building height (H) can be transformed into interval control of H/S to describe the openness of the residential block. Therefore, when designing block ventilation corridors, it is necessary to avoid using a high H/W ratio. The following are recommended optimization parameters: for areas with a lower FAR (approximately 3.0), the H/W ratio should be controlled between 0.7 and 1.0; for areas with a higher FAR (approximately 6.0), the H/W ratio is recommended to be set between 1.3 and 1.6.

4.4.3 Building Geometry Adaptation

To enhance the thermal comfort and air quality of the block, the design of building length and width should balance the needs for shading and ventilation. Sensitivity analysis indicates that the

size ratio of buildings can impact the thermal environment and air circulation. Therefore, in the early stages of block planning, the length-to-width ratio of buildings should be reasonably set in conjunction with the FAR and density. The Pareto front solution set shows that in scenarios with a lower FAR (approximately 3.0), the building length should be between 42 m and 52 m, the width between 26 m and 36 m, the length-to-width ratio between 1.4 and 1.8, and the height between 39 m and 57 m. Such buildings tend to have a combination of slab and tower forms, maintaining the characteristics of slab buildings while being more compact.

In contrast, under the requirement of a higher FAR (approximately 6), the building length is recommended to be between 48 m and 53 m, the width between 42 m and 53 m, the length-to-width ratio between 1.0 and 1.3, and the height range from 75 m to 84 m. This kind of tower-style building, with its larger building volume and height, not only meets the FAR requirements but also ensures an appropriate distance between buildings, promoting ventilation. In summary, for areas pursuing a low FAR, it is recommended to use slab building designs with a length-to-width ratio of about 1.8; for areas with a higher FAR, it is suitable to plan for taller tower-style residences.

4.5. Case Study Application

4.5.1 Improved thermal environment

Field simulations of the optimized morphology demonstrate improvements in outdoor thermal conditions compared to the original design. To validate the practical applicability of the optimization framework and demonstrate real-world performance improvements, the derived morphological strategies were applied to an actual urban renewal project in Shenzhen. The optimization results have been further applied to the case study area. The air temperature distribution at the height of 1.5 m of the case study area is shown in Fig. 12, with ranges between 32 □ and 40 □. Due to the absorption and reflection of solar radiation by building façades, air temperatures near building exteriors were higher, particularly in areas with high building density. In Zones B, C2, and C3, the original building scheme exhibited high density, which hindered heat dissipation from building façades, resulting in the formation of high-temperature zones. In the optimized scheme, increased building spacing enhanced both convective heat transfer and radiative heat exchange on building surfaces. For optimized block, outdoor air temperatures were significantly reduced. In Fig. 12, the red-highlighted regions in Zones B, C2, and C3, where

maximum air temperatures in the original scheme reached up to 38.67 □, experienced air temperature reductions of 4.15 □, 2.92 □, and 4.71 □ under the optimized scheme.

Moreover, in the original scheme, the area near newly constructed high-rise residential complexes exhibited the lowest outdoor air temperatures, likely due to stronger ventilation through narrow gaps and effective shading. In the optimized scheme, the same areas maintained relatively lower outdoor air temperatures, ranging between 31 □ and 34 □. For Zones A, C2, and the public building zone, the average air temperature in the research area under the original scheme was 36.60 □, while the optimized scheme reduced the average temperature by 2.09 □.

(a) Original block (b) Optimized block

Fig. 12 Simulated air temperature contours of the research area

The wind speed within the research area is substantially influenced by morphology. The wind speed distribution at the 1.5 m height cross-section is shown in Fig. 13, where the maximum wind speed reached 5.06 m/s and 4.56 m/s for original and optimized block, respectively. Due to the high building density of the original residential block, continuous street-facing façades were formed on both sides of the streets, resulting in relatively low wind speeds within the research area. Additionally, wind speeds exceeding 5 m/s were observed around the new residential buildings in the original scheme, causing strong slit winds that created discomfort for pedestrians.

Although the optimized design moderately increased the overall wind speed in the area, it strategically redirected airflow through newly added roads, reducing the maximum wind speed in the region to below 5 m/s. In Zones C1, C2, and C3, the original scheme adopted a grid layout with high building density, and the street-facing buildings can obstruct ventilation. This led to large stagnant wind zones (wind speeds of 0-0.2 m/s) in the area. For optimizied block, the increased building spacing widened airflow corridors, allowing more air to flow into the interior of the study area, with most regions achieving wind speeds above 1 m/s.

In particular, in Zone C1, the street-facing buildings channeled wind into the interior of the building clusters, forming wind corridors between buildings. In this plot, the maximum wind speed in the optimized scheme reached 3.28 m/s, representing a significant improvement compared to the original scheme's inter-building wind speed of 0.45 m/s. Additionally, the slit winds around newly constructed high-rise buildings extended to the street, markedly improving ventilation conditions in the stagnant wind zones of the original residential block.

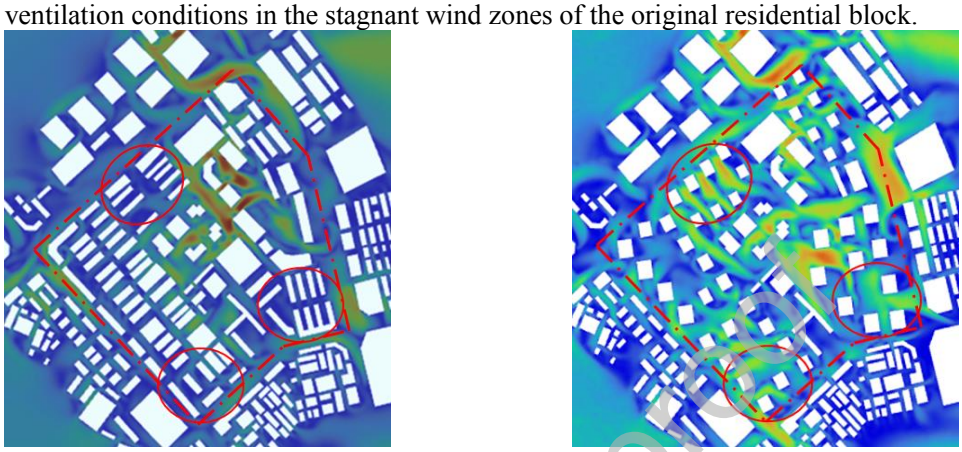

(a) Original block (b) Optimized block

Fig. 13 Simulated wind speed contours of the research area

4.5.2 Improved $PM_{2.5}$ concentration

Beyond thermal improvements, the optimized configuration achieved notable enhancements in air quality through strategic manipulation of wind flow patterns. As shown in Fig. 14, since $PM_{2.5}$ is discrete phase, there are some areas where $PM_{2.5}$ concentrations remain relatively high or near zero. The primary source of pollution in the research area originates from the diffusion of $PM_{2.5}$ from surrounding regions. In the original scheme, the relatively low wind speeds caused $PM_{2.5}$ to accumulate predominantly within the block. The continuous façades of street-facing buildings restricted airflow into the residential block, resulting in lower $PM_{2.5}$ concentrations in the inner areas. Higher wind speeds around the newly constructed residential areas led to relatively elevated $PM_{2.5}$ concentrations. Moreover, in the interior of the building clusters, the optimization increased wind speeds, allowing more outdoor airflow to enter block, which slightly raised $PM_{2.5}$ concentrations. For instance, in Zone B, where wind speeds were low in the original scheme, the optimized scheme increased $PM_{2.5}$ concentration by 5.5 ug/m³ at the same area.

Nevertheless, enhancing ventilation remains crucial for preventing the accumulation of $PM_{2.5}$ within the block. For optimized residential block, the increased wind speeds within the streets facilitated the dispersion of pollutants. This effect was particularly evident on roads adjacent to

Zone C, where areas with reduced $PM_{2.5}$ concentrations corresponded to regions with increased wind speeds. In Zone C1, the original scheme exhibited low wind speeds. However, due to high $PM_{2.5}$ concentrations in nearby streets, pollutant concentrations around buildings in this area were also elevated. For optimized block, $PM_{2.5}$ accumulation in the streets was reduced, and despite higher wind speeds, concentrations in this area decreased distinctly. At the same area, $PM_{2.5}$ concentrations were reduced by 19.66 ug/m^3 under the optimized scheme.

Similarly, near the outer façades of street-facing buildings in Zone C3, $PM_{2.5}$ concentrations decreased by 24.31 ug/m^3 in the optimized scheme. Overall, morphology optimization effectively reduced $PM_{2.5}$ concentrations in areas with severe pollution.

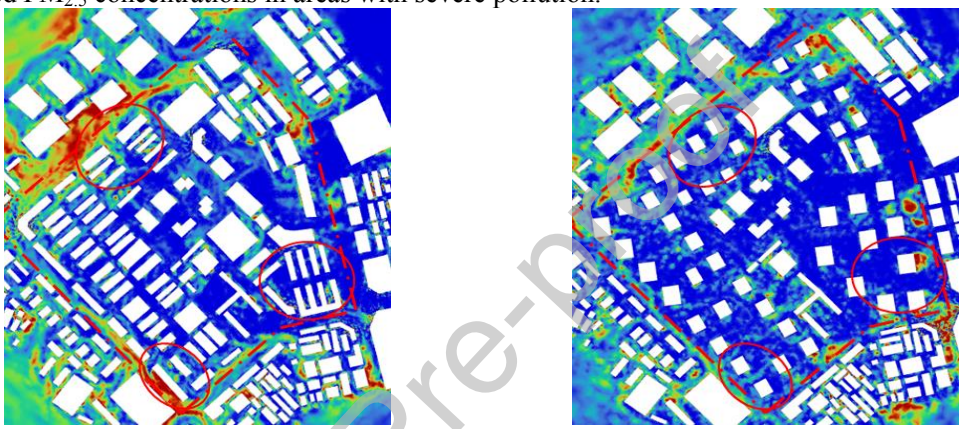

(a) Original block (b) Optimized block

Fig. 14 Simulated $PM_{2.5}$ concentration contours of the research area

4.5.3. Case Study Insights

The comparative analysis between original and optimized designs reveals both the potential benefits and practical considerations for implementing morphological optimization strategies. After in-depth comparative analysis of the optimized schemes, it is evident that optimized scheme demonstrates significant improvements in reducing air temperature, enhancing wind speeds, and lowering $PM_{2.5}$ concentrations. Tshis study employs a combination of numerical simulations, parametric modeling, and multi-objective optimization to propose a computational design approach for the morphology of residential block. This approach effectively integrates considerations of thermal environment and air quality, showcasing high feasibility and effectiveness.

However, the results obtained from the numerical simulations also highlight potential issues within the physical environment of the block. To further improve block optimization design, the following aspects should be prioritized:

(1) Mitigating high-speed wind tunnels between tall and super-tall buildings

For densely built clusters of tall and super-tall buildings, rational planning of surrounding building layouts is essential to create smooth airflow channels. This would help direct ventilation while reducing localized high wind speeds. In areas awaiting redevelopment, efforts should focus on widening ventilation corridors as much as possible, while ensuring compliance with building density and floor area ratio requirements, to effectively prevent the formation of high-speed wind.

(2) Avoiding outdoor activity areas in highly polluted zones

While morphology optimization can significantly enhances ventilation, it can also lead to increased diffusion of air pollutants from surrounding areas into the block interior. Particularly in vortex zones behind buildings, turbulence and eddies often result in elevated concentrations of air pollutants. Wind field analyses should guide adjustments to building layouts to minimize vortex zones. During detailed block design, it is essential to accurately identify areas with high $PM_{2.5}$ concentrations and avoid overlapping outdoor activity spaces with polluted areas.

5 Discussions

5.1 Key Findings and Comparison with Previous Research

This study's integrated optimization framework reveals several important findings that both confirm and extend previous research on urban morphology optimization. The two-way coupled model demonstrates that thermal environment and air quality exhibit complex interdependencies that single-objective studies cannot capture effectively.

The optimal building orientation results align with established ventilation principles, with angles less than 15° to prevailing winds proving most effective for both thermal comfort and air quality. This finding corroborates García et al. [42] who demonstrated the positive role of parallel wind directions in facilitating PM dispersion, while extending their work by quantifying the thermal comfort benefits simultaneously. However, our results contradict studies suggesting 45° angles are optimal for PM dispersion [21], likely due to our consideration of thermal environment interactions and local emission sources.

Building height effects show more complex relationships than previously reported. While deep urban canyons (H/W > 2) effectively reduce thermal stress through shading [19], our results demonstrate they simultaneously elevate $PM_{2.5}$ concentrations, consistent with Miao et al. [17]

who found PM concentrations are higher in deep versus balanced canyons. The optimal H/W ratios identified in this study (0.7-1.0 for low FAR, 1.3-1.6 for high FAR) represent a compromise between these competing effects, providing new quantitative guidance for practitioners.

The sensitivity analysis reveals that longitudinal spacing (aligned with wind direction) has the greatest impact on both objectives, with correlation coefficients of ±0.81. This finding extends Kurppa et al. [76] who recommended lower H/W values for PM reduction, by demonstrating that spacing orientation matters more than absolute dimensions. The minimal impact of transverse spacing contradicts conventional wisdom about cross-ventilation but aligns with computational studies showing that wind-aligned corridors dominate pollutant dispersion patterns.

5.2 Methodological Contributions and Validation

Beyond the specific morphological findings, this research advances urban environmental modeling methodology through its coupled simulation-optimization framework. The RSM-based optimization approach successfully bridges the gap between computationally intensive CFD modeling and practical design applications. With R^2 values of 0.98-0.99 and maximum errors below 8.13%, the surrogate model demonstrates superior accuracy compared to typical urban design approximations while reducing computational time by orders of magnitude. This addresses a critical limitation identified by Li et al. [45], who noted the lack of systematic optimization frameworks for residential block planning.

The two-way coupling mechanism represents a significant advance over conventional one-way models. By incorporating $PM_{2.5}$ effects on radiative transfer and momentum exchange, the model captures thermal-pollutant interactions that previous studies overlooked. Case study conducted for Shenzhen demonstrates the model's predictive capability. The reduction of air temperature by 2.09°C and improved air circulation were achieved while maintaining development density requirements.

The results of the Pareto optimization indicate trade-offs inherent between thermal comfort and air quality that sheds light on conflicting recommendations found in earlier literature sources. The prioritization of UTCI settings usually comes at the expense of air quality and vice versa, showing why one-objective techniques supply conflicting advice. The determination of two different ranges of parameter intervals that represent various ranges of FAR has practical

flexibility to the designers without compromising environmental performance.

5.3 Practical Implications for Urban Design

The quantitative relationships and optimization strategies identified in this study should be translated into specific design recommendations that can inform planning practice and regulatory frameworks. The optimization strategies developed provide evidence-based alternatives to conventional planning approaches. The recommendation for building orientations within 15° of prevailing winds directly challenges traditional north-south orientation mandates in many planning codes, particularly where site conditions or street layouts make such orientations impractical. The flexible H/W ratio guidelines (0.7-1.6 depending on FAR) offer more nuanced design guidance than existing binary recommendations for "compact" versus "open" urban forms.

For regulatory framework updates, planners should implement graduated H/W ratios based on development density: 0.7-1.0 for low-density zones (FAR 3.0-4.0), 1.0-1.3 for medium-density (FAR 4.0-5.0), and 1.3-1.6 for high-density zones (FAR 5.0-6.0). Longitudinal spacing parallel to prevailing winds should be prioritized with minimum requirements 1.5 times transverse spacing, acknowledging its dominant influence (correlation ±0.81) on both thermal comfort and air quality.

Building typology selection should adapt to density constraints: slab buildings with length-to-width ratios ~1.8 for low FAR areas (<4.0) and tower configurations with ratios 1.0-1.3 for high FAR areas (>5.0). This differentiation optimizes environmental performance while maintaining development viability. Performance verification through CFD modeling should be required at key design stages, with environmental performance bonuses (FAR increases of 0.2-0.5) offered for developments achieving UTCI reductions >2°C and maintaining $AQI_{PM2.5}$ < 50.

Nonetheless, policy innovation is necessary because of implementation challenges. The existing setback operations and orientation limitations tend to contradict the most appropriate designs. Economic barriers to the adoption of larger spacing requirements can be removed through environmental performance-based incentives, such as fast-track approvals of pre-validated morphologies and access to green financing.

5.4 Open Questions and Future Research Directions

While this study advances integrated environmental optimization, several fundamental

questions remain unresolved, highlighting both the contributions and boundaries of current knowledge. Even with the progress in urban environmental modeling in this study, there are several basic questions that lack answers, and this aspect evidences the contributions and limitations of this study.

The paradox of the coupling: How does one city design optimize both thermal comfort by compact forms and air quality by open ventilation of the design? The coupled model used in our study shows that there is no single-point solution to this paradox, but trade-offs must be accepted. The Pareto front analysis shows that there is a trade-off relationship between the two objectives, in the sense that to increase one, the other has to be degraded, even though the best trade-offs are context-dependent.

Climate and transferability: Are the morphological optimization principles that have been determined on the block scale suitable to the district or city scale, and to what extent are morphological optimization results transferable between climates? Though our framework will offer blockwise optimization in hot-humid climates, larger-scale aggregation issues and adjustment to alternative climatic scenarios will necessitate a recalibration of the model. The approach is portable, though the best morphologies will probably vary widely among climates.

Temporal robustness: Can static optimization adequately address dynamic environmental conditions? Our steady-state model only contains average circumstances, and which cannot be sure of the performance in a severe event and in diurnal and seasonal changes. Follow-up studies ought to come up with computationally feasible dynamic optimization methods that take into consideration variability over time.

Geometric complexity: What is the difference between optimized results assuming realistic urban heterogeneity and idealized geometries? Our simplified grid typology can do systematic analysis, but may not be able to represent all the complexities of mixed-use schemes, odd building layout and different topographic situations. Generalisation to more sophisticated geometries is an urgent issue.

Multi-pollutant and multi-objective expansion: How does one extend strategies to take into account other pollutants and other objectives beyond $PM_{2.5}$, and thermal comfort and air quality? Alignment with building energy use, gains of green infrastructure, and multiple pollutant species may also change optimal configurations in a fundamental way. Such extensions can be based on

the framework, but the computational demands and trade-off complexity will grow substantially.

Validation at long run: What is the performance of optimized designs under real-world implementation over long durations? Although the short-term advantages are evident in our case study, the long-term observation of the projects constructed in accordance with these guidelines would enhance the trust in the methodology and the possibility to continuously improving it.

These unresolved questions outline the course of subsequent research by recognizing that a full understanding might still depend upon some breakthroughs in methods of computational modelling, changes in monitoring technologies, and even our knowledge of urban environmental systems. The methodological framework and quantitative implications of this study contribute to the area by conceptualizing a level of knowledge that contributes to a solution to these broader issues.

5.5 Policy Recommendations

Drawing from the technical findings and practical insights, the following policy recommendations target different stakeholders in the urban development process. On the basis of our results, we would like to make the following tangible policy recommendations to various stakeholders:

For Urban Planning Departments: Eliminate prescriptive building orientation and replace with performance standards that offer density differentiated spacing requirements, H/W of 0.7-1.0 on FAR 3.0-4.0, 1.0-1.3 on FAR 4.0-5.0 and 1.3-1.6 on FAR 5.0-6.0. Require residential projects with floorspace greater than 10,000 m2 to undergo environmental impact assessments via validated CFD models to guarantee both UTCI and $AQI_{PM2.5}$ targets, prior to authorization.

For Environmental Protection Agencies: Include air quality issues in building regulations by mandating a minimum longitudinal spacing 1.5 times the transverse separation along the prevailing wind directions. Put in place monitoring guidelines that monitor the thermal comfort and the $PM_{2.5}$ concentration at pedestrian level in the developments, one year after construction has been completed. Design publicly available databases of tested morphological arrangements that attain two environmental goals to inform future developments.

For Engineering consultants: Integrate two-way coupled CFD-RSM framework to use in environmental assessment and no longer on single-objective studies. Apply the given ranges of

parameters and sensitivity coefficients to make quick preliminary evaluations when performing conceptual design. Apply iterative optimization in the design development stage, aiming to become Pareto-optimal solutions, trade-offs between client density conditions and environmental performance.

For Municipal Governments: Implement new tiered incentive rates of 0.2-0.5 FAR bonuses on developments that have shown UTCI reduction > 2 □ and $AQI_{PM2.5}$ < 50 achieved through validated modeling. Provide fast-track permitting with up to 30 percent reduction in permitting time when the morphological configurations are pre-validated. Couple the environmental optimization compliance with green bonds eligibility and preferential loan rates to counter higher construction costs incurred due to provision of larger spacing.

For Professional Associations: Revise design guidelines to make integrated thermal-air quality optimization a regular practice. Come up with professional certification programs in multi-objective optimization and coupled environmental modeling. Peer review systems can be created over CFD validations studies in order to impose consistency and reliability of projects.

The above policy suggestions that can be implemented as practical courses of action that ensure the preservation of the viability of development through systematic enhancement of urban environmental quality. The process of implementation can start by pilot projects in new development zones and be gradually integrated into the comprehensive planning frameworks which will be based on monitored performance results.

6 Conclusion

This study develops an integrated optimization framework for residential block morphology that simultaneously addresses thermal comfort and air quality through a novel two-way coupled numerical model. The methodology successfully bridges physics-driven CFD simulation with data-driven optimization techniques, providing practical design guidance for hot-humid climates. The key findings from this research include:

• Building orientation within 15° of prevailing winds provides optimal environmental performance for both thermal comfort and air quality

• Longitudinal spacing (wind-aligned corridors) exhibits the strongest influence on both UTCI and $AQI_{PM2.5}$ (correlation coefficient ±0.81)

• Optimal height-to-width ratios depend on development density: 0.7-1.0 for low FAR (~3) and 1.3-1.6 for high FAR (~6)

• Slab-type buildings (length-to-width ratio ~1.8) suit low-density areas while tower-type configurations (ratio 1.0-1.3) optimize high-density developments

• Response surface modeling achieves 95% accuracy (R^2 = 0.98-0.99) while reducing computational requirements by orders of magnitude

• Case study demonstrates air temperature reductions up to 2.09°C with improved wind circulation while maintaining regulatory compliance

The optimization framework reveals fundamental trade-offs between thermal comfort and air quality that explain contradictory recommendations in previous literature. The methodology provides quantitative tools for evidence-based design decisions while accommodating practical constraints including regulatory requirements and economic considerations. This integrated approach offers urban planners and designers practical tools for creating healthier residential environments while maintaining development viability. The computational accessibility through response surface modeling enables adoption without specialized CFD expertise. Future research should extend the methodology to different climatic conditions and integrate with green infrastructure systems, while policy development should focus on performance-based regulations that reward environmental outcomes alongside traditional density criteria.

Reference

[1] Shen P, Yang B. Projecting Texas energy use for residential sector under future climate and urbanization scenarios: A bottom-up method based on twenty-year regional energy use data. Energy. 2020;193:116694.

[2] Dong W, Dai D, Liu M, Wang Y, Li S, Shen P. Combined effects of the visual-thermal environment on restorative benefits in hot outdoor public spaces: A case study in Shenzhen, China. Building and Environment. 2025;272:112690.

[3] Shen P, Ji Y, Li Y, Wang M, Cui X, Tong H. Combined impact of climate change and heat island on building energy use in three megacities in China. Energy and Buildings. 2025:115386.

[4] Shen P, Wang M, Ma H, Ma N. On the two-way interactions of urban thermal environment and air pollution: A review of synergies for identifying climate-resilient mitigation strategies. Building Simulation. 2025;18:259–79.

[5] Mika J, Forgo P, Lakatos L, Olah AB, Rapi S, Utasi Z. Impact of 1.5 K global warming on urban air pollution and heat island with outlook on human health effects. Curr Opin Env Sust. 2018;30:151-9.

[6] Yu YC, Liu JL, Chauhan K, de Dear R, Niu JL. Experimental study on convective heat transfer coefficients for the human body exposed to turbulent wind conditions. Building and Environment. 2020;169:106533.

[7] Haines A, Kovats RS, Campbell-Lendrum D, Corvalan C. Climate change and human health: Impacts, vulnerability and public health. Public Health. 2006;120:585-96.

[8] Ma X, Fukuda H, Zhou DA, Wang MY. Study on outdoor thermal comfort of the commercial pedestrian block in hot-summer and cold-winter region of southern China-a case study of The Taizhou Old Block. Tourism Manage. 2019;75:186-205.

[9] Statistics ABo. Feature article: the exceptional heatwave of january-february 2009 in south-eastern australia. 2009.

[10] Chhabra SK. Air pollution and health. Indian Journal of Chest Diseases Allied Ences. 2002;44:8-9.

[11] Raaschou-Nielsen O, Andersen ZJ, Beelen R, Samoli E, Stafoggia M, Weinmayr G, et al. Air pollution and lung cancer incidence in 17 European cohorts: prospective analyses from the European Study of Cohorts for Air Pollution Effects (ESCAPE). Lancet Oncol. 2013;14:813-22.

[12] Seaton A, Macnee W, Donaldson K, Godden D. Particulate Air-Pollution and Acute Health-Effects. Lancet. 1995;345:176-8.

[13] He KB, Huo H, Zhang Q. Urban air pollution in China: Current status, characteristics, and progress. Annu Rev Energ Env. 2002;27:397-431.

[14] Abdulkareem AS, Odigure JO, Abenege S. Predictive Model for Pollutant Dispersion from Gas Flaring: A Case Study of Oil Producing Area of Nigeria. Energ Source Part A. 2009;31:1004-15.

[15] WHO. Air pollution. World Health Organization; 2022.

[16] EPA. Outdoor Air Quality. What are the trends in outdoor air quality and their effects on human health and the environment?: United States Environmental Protection Agency; 2022.

[17] Miao C, Yu S, Hu Y, Bu R, Qi L, He X, et al. How the morphology of urban street canyons affects suspended particulate matter concentration at the pedestrian level: An in-situ investigation. Sustainable Cities and Society. 2020;55:102042.

[18] Cui X, Li Y, Shen P. Beyond CFD: explainable machine learning for efficient assessment of urban morphology impacts on pedestrian level wind and thermal environment. Journal of Building Performance Simulation. 2025;2025/05/25:1-16.

[19] Shen P, Li Y, Gao X, Chen S, Cui X, Zhang Y, et al. Climate Adaptability of Building Passive Strategies to Changing Future Urban Climate: A Review. Nexus. 2025;2:1-13.
[20] Johansson E, Spangenberg J, Gouvêa ML, Freitas ED. Scale-integrated atmospheric simulations to assess thermal comfort in different urban tissues in the warm humid summer of São Paulo, Brazil. Urban Climate. 2013;6:24-43.
[21] Ahmad K, Khare M, Chaudhry KK. Wind tunnel simulation studies on dispersion at urban street canyons and intersections - A review. Journal of Wind Engineering and Industrial Aerodynamics. 2005;93:697-717.
[22] Shashua-Bar L, Tzamir Y, Hoffman ME. Thermal effects of building geometry and spacing on the urban canopy layer microclimate in a hot-humid climate in summer. International Journal of Climatology. 2010;24:1729–42.
[23] Bourbia F, Boucheriba F. Impact of street design on urban microclimate for semi arid climate (Constantine). Renewable Energy. 2010;35:343-7.
[24] Jung S, Yoon S. Analysis of the Effects of Floor Area Ratio Change in Urban Street Canyons on Microclimate and Particulate Matter. Energies. 2021;14:714.
[25] Geros V, Santamouris M, Karatasou S, Tsangrassoulis A, Papanikolaou N. On the cooling potential of night ventilation techniques in the urban environment. Energy and Buildings. 2005;37:243-57.
[26] Lin L, Hang J, Wang X, Wang X, Fan S, Fan Q, et al. Integrated Effects of Street Layouts and Wall Heating on Vehicular Pollutant Dispersion and their Reentry Toward Downstream Canyons. Aerosol and Air Quality Research. 2016;16:3142-63.
[27] Andreou E. Thermal comfort in outdoor spaces and urban canyon microclimate. Renewable energy. 2013;55:182-8.
[28] Dong W, Dai D, Shen P, Zhang R, Liu M. How Public Urban Space Enhance Restoration Benefits Through Combined Multisensory Effects: A Systematic Review. Land. 2024;13:2018.
[29] Abreu-Harbich LV, Labaki LC, Matzarakis A. Thermal bioclimate in idealized urban street canyons in Campinas, Brazil. Theoretical Applied Climatology. 2014;115:333–40.
[30] Ji Y, Song J, Shen P. A review of studies and modelling of solar radiation on human thermal comfort in outdoor environment. Building and Environment. 2022;214:108891.
[31] Ji Y, Song J, Shen P. A data-driven model on human thermophysiological and psychological responses under dynamic solar radiation. Building and Environment. 2024;248:111098.
[32] Shashua-Bar L, Hoffman ME. Quantitative evaluation of passive cooling of the UCL microclimate in hot regions in summer, case study: urban streets and courtyards with trees. Building and Environment. 2004;39:1087-99.
[33] Krüger E, Pearlmutter D, Rasia F. Evaluating the impact of canyon geometry and orientation on cooling loads in a high-mass building in a hot dry environment. Applied Energy. 2010;87:2068-78.
[34] Georgakis C, Santamouris M. On the air flow in urban canyons for ventilation purposes. International Journal of Ventilation. 2004;V3:53-65.
[35] Offerle B, Eliasson I, Grimmond CSB, Holmer B. Surface heating in relation to air temperature, wind and turbulence in an urban street canyon. Boundary-Layer Meteorology. 2007;122:273-92.
[36] Jamei E, Rajagopalan P, Seyedmahmoudian M, Jamei Y. Review on the impact of urban geometry and pedestrian level greening on outdoor thermal comfort. Renewable & Sustainable Energy Reviews. 2016;54:1002-17.
[37] Niachou K, Livada I, Santamouris M. Experimental study of temperature and airflow distribution

inside an urban street canyon during hot summer weather conditions. Part II: Airflow analysis. Building and Environment. 2008;43:1393-403.

[38] Santamouris M, Papanikolaou N, Koronakis I, Livada I, Asimakopoulos D. Thermal and air flow characteristics in a deep pedestrian canyon under hot weather conditions. Atmospheric Environment. 1999;33:4503-21.

[39] Hahn I, Brixey LA, Wiener RW, Henkle SW, Baldauf R. Characterization of traffic-related PM concentration distribution and fluctuation patterns in near-highway urban residential street canyons. J Environ Monit. 2009;11:2136-45.

[40] Weber S, Kuttler W, Weber K. Flow characteristics and particle mass and number concentration variability within a busy urban street canyon. Atmos Environ. 2006;40:7565-78.

[41] Buccolieri R, Jeanjean APR, Gatto E, Leigh RJ. The impact of trees on street ventilation, NOx and PM2.5 concentrations across heights in Marylebone Rd street canyon, central London. Sustainable Cities and Society. 2018;41:227-41.

[42] García J, Cerdeira R, Tavares N, Coelho LMR. Studying street geometry influence in PM 10 concentration. International Journal of Environment Pollution. 2012;50:283.

[43] Yang Z, Peng J, Jiang S, Yu X, Hu T. Optimizing building spatial morphology to alleviate human thermal stress. Sustainable Cities and Society. 2024;106:105386.

[44] da Silva FT, Reis NC, Santos JM, Goulart EV, de Alvarez CE. Influence of urban form on air quality: The combined effect of block typology and urban planning indices on city breathability. Science of The Total Environment. 2022;814:152670.

[45] Li Z, Zhang H, Wen C-Y, Yang A-S, Juan Y-H. Effects of frontal area density on outdoor thermal comfort and air quality. Building and Environment. 2020;180:107028.

[46] Tominaga Y, Stathopoulos T. CFD simulation of near-field pollutant dispersion in the urban environment: A review of current modeling techniques. Atmospheric Environment. 2013;79:716-30.

[47] Nazarian N, Kleissl J. CFD simulation of an idealized urban environment: Thermal effects of geometrical characteristics and surface materials. Urban Climate. 2015;12:141-59.

[48] Toparlar Y, Blocken B, Maiheu B, van Heijst GJF. A review on the CFD analysis of urban microclimate. Renewable and Sustainable Energy Reviews. 2017;80:1613-40.

[49] Shen P, Braham W, Yi Y. The feasibility and importance of considering climate change impacts in building retrofit analysis. Applied Energy. 2019;233-234:254-70.

[50] Shen P. Building retrofit optimization considering future climate and decision-making under various mindsets. Journal of Building Engineering. 2024;96:110422.

[51] Zaid H, Al-sharify Z, Hamzah MH, Rushdi S. Optimization Of Different Chemical Processes Using Response Surface Methodology- A Review: Response Surface Methodology. Journal of Engineering and Sustainable Development. 2022;26:1-12.

[52] Westermann P, Evins R. Surrogate modelling for sustainable building design – A review. Energy and Buildings. 2019;198:170-86.

[53] Du Y, Mak CM, Liu J, Xia Q, Niu J, Kwok KCS. Effects of lift-up design on pedestrian level wind comfort in different building configurations under three wind directions. Building and Environment. 2017;117:84-99.

[54] Gousseau P, Blocken B, van Heijst GJF. CFD simulation of pollutant dispersion around isolated buildings: On the role of convective and turbulent mass fluxes in the prediction accuracy. Journal of Hazardous Materials. 2011;194:422-34.

[55] Wang M, Ma H, Zheng X, Han C, Shen P. Two-way coupled numerical simulation between outdoor thermal environment and PM2.5 in residential blocks. Building and Environment. 2025;275:112821.
[56] Allegrini J, Dorer V, Carmeliet J. Coupled CFD, radiation and building energy model for studying heat fluxes in an urban environment with generic building configurations. Sustainable Cities and Society. 2015;19:385-94.
[57] Srebric J, Heidarinejad M, Liu J. Building neighborhood emerging properties and their impacts on multi-scale modeling of building energy and airflows. Building and Environment. 2015;91:246-62.
[58] Bouyer J, Inard C, Musy M. Microclimatic coupling as a solution to improve building energy simulation in an urban context. Energy and Buildings. 2011;43:1549-59.
[59] Reinhart CF, Cerezo Davila C. Urban building energy modeling – A review of a nascent field. Building and Environment. 2016;97:196-202.
[60] Shen P, Wang Z. How neighborhood form influences building energy use in winter design condition: Case study of Chicago using CFD coupled simulation. Journal of Cleaner Production. 2020;261:121094.
[61] Vermeulen T, Knopf-Lenoir C, Villon P, Beckers B. Urban layout optimization framework to maximize direct solar irradiation. Computers, Environment and Urban Systems. 2015;51:1-12.
[62] Blocken B. Computational Fluid Dynamics for urban physics: Importance, scales, possibilities, limitations and ten tips and tricks towards accurate and reliable simulations. Building and Environment. 2015;91:219-45.
[63] Salvati A, Coch H, Morganti M. Effects of urban compactness on the building energy performance in Mediterranean climate. Energy Procedia. 2017;122:499-504.
[64] Javanroodi K, Mahdavinejad M, Nik VM. Impacts of urban morphology on reducing cooling load and increasing ventilation potential in hot-arid climate. Applied Energy. 2018;231:714-46.
[65] Błażejczyk K, Broede P, Fiala D, Havenith G, Holmér I, Jendritzky G, et al. Principles of the new Universal Thermal Climate Index (UTCI) and its application to bioclimatic research in European scale. 2010;14:91-102.
[66] China MoEPo. Ambient air quality standards GB 3095—2012. Ministry of Environmental Protection of China; 2012. p. 2.
[67] Xu Y, Ren C, Ma P, Ho J, Wang W, Lau KK-L, et al. Urban morphology detection and computation for urban climate research. Landscape and Urban Planning. 2017;167:212-24.
[68] Shareef S. The impact of urban morphology and building's height diversity on energy consumption at urban scale. The case study of Dubai. Building and Environment. 2021;194:107675.
[69] Yang S, Zhou D, Wang Y, Li P. Comparing impact of multi-factor planning layouts in residential areas on summer thermal comfort based on orthogonal design of experiments (ODOE). Building and Environment. 2020;182:107145.
[70] Xu S, Wang S, Li G, Zhou H, Meng C, Qin Y, et al. Performance-based design of residential blocks for the co-benefits of building energy efficiency and outdoor thermal comfort improvement. Building and Environment. 2024;264:111926.
[71] Yu Y, Kwok KCS, Liu XP, Zhang Y. Air pollutant dispersion around high-rise buildings under different angles of wind incidence. Journal of Wind Engineering and Industrial Aerodynamics. 2017;167:51-61.
[72] Liu B, Liu Y, Cho S, Chow DHC. Urban morphology indicators and solar radiation acquisition:

2011–2022 review. Renewable and Sustainable Energy Reviews. 2024;199:114548.
[73] Government SMPs. Shenzhen Urban Planning Standards and Guidelines. 2021. p. 27-127.
[74] Hastie TJ. Generalized additive models. Statistical models in S. 2017:249-307.
[75] Cleveland WS, Devlin SJ. Locally Weighted Regression: An Approach to Regression Analysis by Local Fitting. Journal of the American Statistical Association. 1988;83:596-610.
[76] Kurppa M, Hellsten A, Auvinen M, Raasch S, Vesala T, Vesala T, et al. Ventilation and Air Quality in City Blocks Using Large-Eddy Simulation Urban Planning Perspective. Atmosphere. 2018;9:65.

Appendix:

A.1 Computational Domain and Mesh Configuration

A.1.1 Geometric Model Setup

The computational fluid dynamics simulations were performed using ANSYS Fluent 19.2. The computational domain was constructed based on electronic map data and field survey information, with building geometries simplified to enhance computational efficiency while preserving essential morphological characteristics. All building openings (doors and windows) were modeled as closed surfaces to represent typical daytime operating conditions. The simplified geometric model of the target area including the distribution of measurement points is illustrated in Figure A.1.

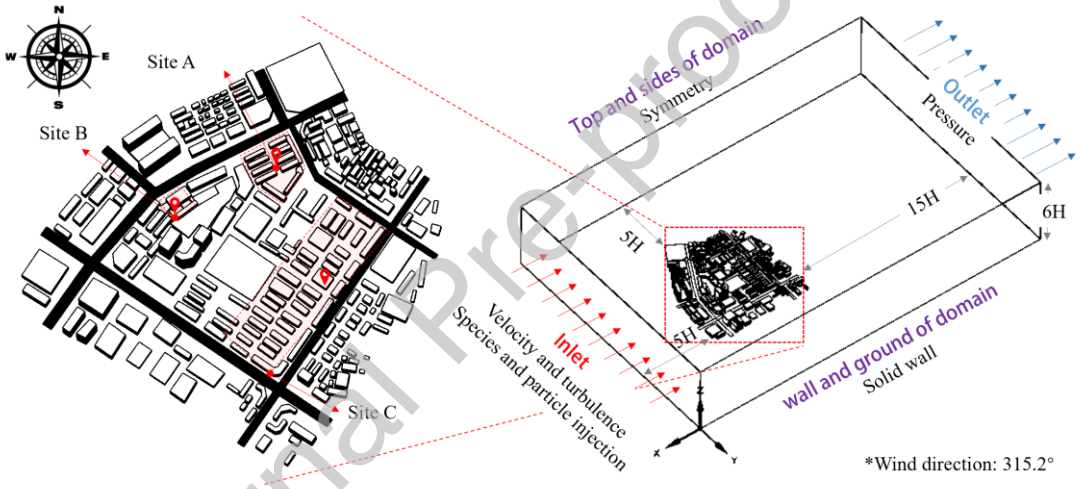

Figure A.1 Geometric model of the target area

The computational domain dimensions were established following established best practices for urban CFD studies. Specifically, boundaries were positioned at minimum distances of 5H from the study area, where H represents the maximum building height. The inlet boundary was located 5H upstream, the outlet boundary 15H downstream, and the top boundary 6H above the tallest building to minimize blockage effects and ensure proper flow development.

A.1.2 Boundary Condition Classification

Boundary conditions were configured separately for the continuous phase (air) and discrete phase (PM□.□) according to established urban CFD protocols. The detailed boundary condition specifications are presented in Table A.1.

Table A.1 Boundary conditions for numerical model

Boundary	**Continuous Phase**	**Discrete Phase**
Inlet	Velocity inlet	Escape
Road surfaces	Interior	Escape
Outlet	Pressure outlet	Escape
Building walls/Ground	Wall (no-slip)	Reflect
Domain top/sides	Symmetry	Symmetry

The continuous phase boundary conditions follow standard practices for urban atmospheric flow modeling, with velocity inlet conditions applied to prescribe logarithmic wind profiles and pressure outlet conditions to allow natural flow development. For the discrete phase, escape boundaries were specified at inlet, road surfaces, and outlet to allow particle injection and removal, while reflect boundaries at solid surfaces simulate particle-wall interactions.

A.1.3 Mesh Generation and Quality Control

A tetrahedral mesh was employed to accommodate the complex building geometries within the urban environment. The mesh configuration parameters were established based on grid independence studies and computational resource constraints:

- Building and road surfaces: 5 m characteristic length
- Ground surface mesh: 5 m characteristic length
- Domain boundaries: 10 m characteristic length
- Maximum cell size within domain: 15 m
- Growth rate: 1.1
- Boundary layer mesh: first layer height 0.1 m, growth rate 1.1, 10 layers total

The final computational mesh contained 31.12 million cells with a minimum orthogonal quality of 0.10, maximum aspect ratio of 336, and y□ values maintained below 800 at all wall surfaces to ensure adequate near-wall resolution for the selected turbulence model.

A.2 Model Setup and Physical Parameters

A.2.1 Meteorological Input Parameters

Field measurements were collected for September 28, 2021, utilizing data from the Shenzhen government open data platform (https://opendata.sz.gov.cn) and local environmental monitoring stations. The comprehensive hourly meteorological parameters including wind velocity and direction, air temperature and humidity, solar radiation components, and PM□.□ concentrations

are presented in Figure A.2.

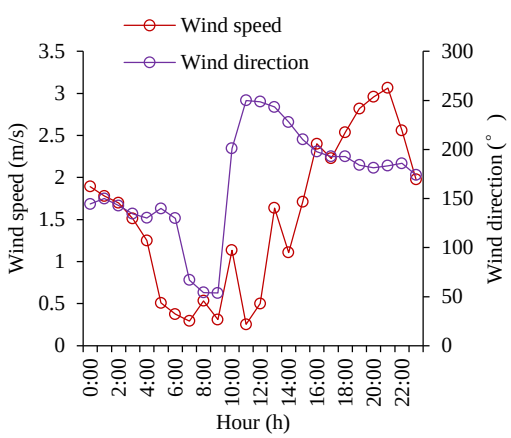

(a) Wind velocity and direction (The north is 0°)

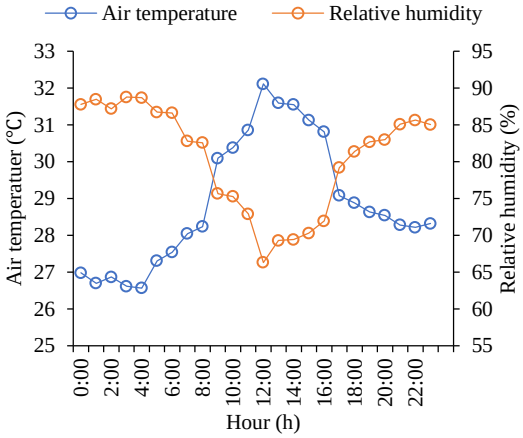

(b) Air temperature and humidity

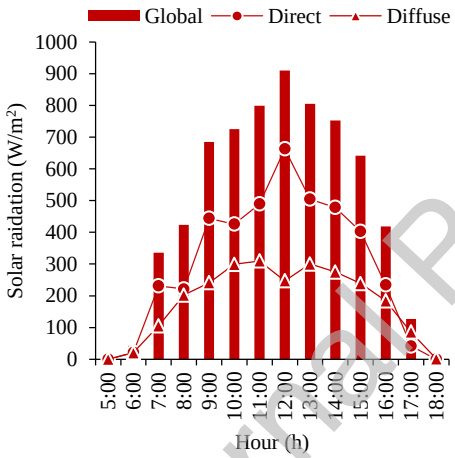

(c) Solar radiation

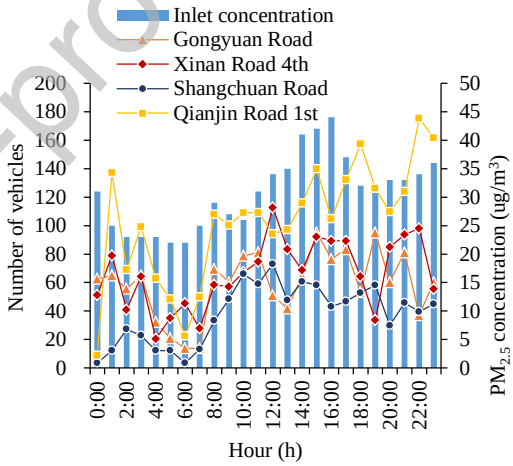

(d) $PM_{2.5}$ concentrations

Figure A.2 Inlet parameters of target area: (a) Wind velocity and direction (The north is 0°), (b) Air temperature and humidity, (c) Solar radiation, (d) PM□.□ concentrations

The wind velocity profile was prescribed as a logarithmic function typical of atmospheric boundary layer flows over urban terrain. The meteorological data represents typical summer pollution conditions in the subtropical climate of Shenzhen, with elevated temperatures and moderate PM□.□ concentrations suitable for model validation purposes.

A.2.2 Material Properties and Heat Transfer

Surface material properties were specified according to typical urban construction materials

and established literature values. The thermal and radiative properties are summarized in Table A.2. The convective heat transfer coefficient at building surfaces was calculated as a function of local wind speed using the empirical correlation:

$$h_c = 5.7 + 3.8u \quad \text{(A.1)}$$

where h_c is the convective heat transfer coefficient (W/m²·K) and u is the local wind speed (m/s).

Table A.2 Material properties for model surfaces

Surface	Absorptivity	Emissivity	Specific Heat (J/kg·K)	Density (kg/m³)	Thermal Conductivity (W/m·K)	Thickness (m)
Ground/Road	0.6	0.95	880	2600	2.0	0.15
Building walls	0.6	0.7	750	2400	1.5	0.24

A.2.3 Anthropogenic Heat Sources

Building heat rejection from air conditioning systems was modeled as distributed internal heat sources on exterior wall surfaces, representing the thermal impact of building mechanical systems on the outdoor environment. Heat load calculations were performed according to Chinese residential building energy efficiency standards (JGJ75-2012) with the following specifications:

- Window-to-wall ratios: North facade 0.45, East/West facades 0.3, South facade 0.5
- Overall building envelope heat transfer coefficient: 1.5 W/(m²·K)
- Indoor design temperature: 26°C
- Window overall heat transfer coefficient: 2.0 W/(m²·K)
- Solar heat gain coefficient: 0.6

The calculated hourly anthropogenic heat emissions exhibit significant diurnal variation, ranging from less than 50 W/m² during nighttime hours to exceeding 140 W/m² during peak afternoon conditions, as illustrated in Figure A.3.

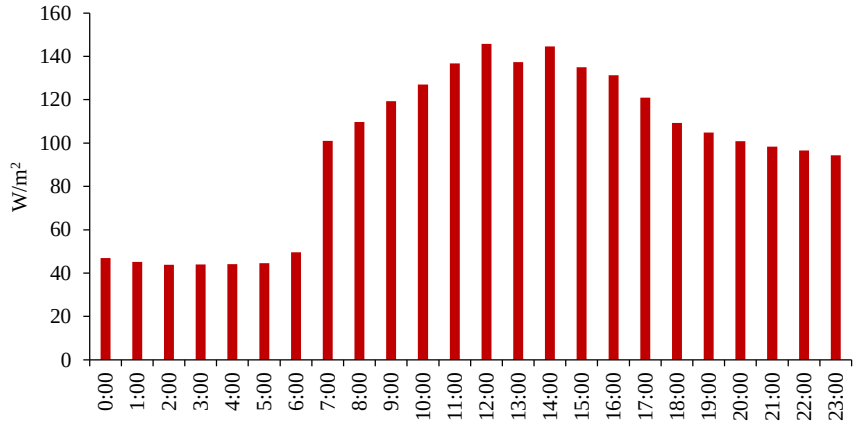

Figure A.3 Hourly anthropogenic heat emission from buildings

A.2.4 PM□.□ Emission Sources

Vehicle-generated PM□.□ emissions were calculated using methodologies prescribed in the Chinese technical guidelines for mobile source emission inventories. The emission rate calculation employed the following formulation:

$$E_1 = \sum_i B_i \times EF_i \times VKT_i \times 10^{-6}$$

(A.2)

where E□ represents the annual PM□.□ emission rate (kg), B_i is the number of vehicles of type i, EF_i is the emission factor (g/km), and VKT_i is the vehicle kilometers traveled per year (km/vehicle).

The emission factor was calculated as:

$$EF_{i,j} = BEF_i \times \varphi_j$$

(A.3)

where BEF_i is the base emission factor (0.003 g/km for gasoline vehicles) and φ□ is the meteorological correction factor (0.8372). Vehicle operating conditions assumed an average speed of 30 km/h and annual mileage of 18,000 km per vehicle.

A.3 Numerical Solution Methodology

A.3.1 Governing Equations and Turbulence Modeling

The numerical model employs the steady-state three-dimensional Reynolds-Averaged Navier-Stokes (RANS) equations for incompressible turbulent flow. The continuity equation for incompressible flow is expressed as:

$$\frac{\partial u_i}{\partial x_i} = 0$$

(A.4)

The momentum conservation equation incorporating the Boussinesq approximation for buoyancy effects is written as:

$$\frac{\partial(u_i u_j)}{\partial x_j} = -\frac{1}{\rho}\frac{\partial p}{\partial x_i} + \frac{\partial}{\partial x_j}\left[(\nu + \nu_t)\left(\frac{\partial u_i}{\partial x_j} + \frac{\partial u_j}{\partial x_i}\right)\right] + g_i\beta(T - T_0)$$

(A.5)

where u_i are the velocity components, p is pressure, ρ is density, ν is molecular viscosity, ν□ is turbulent viscosity, g_i are gravitational acceleration components, β is the thermal expansion coefficient, T is temperature, and T□ is the reference temperature.

The RNG k-ε turbulence model was selected for closure of the Reynolds stress terms due to its superior performance in urban flow simulations with adverse pressure gradients and flow separation. The transport equations for turbulent kinetic energy (k) and dissipation rate (ε) are:

$$\frac{\partial(\rho k u_i)}{\partial x_i} = \frac{\partial}{\partial x_j}\left[\left(\mu + \frac{\mu_t}{\sigma_k}\right)\frac{\partial k}{\partial x_j}\right] + G_k + G_b - \rho$$

(A.6)

$$\frac{\partial(\rho\varepsilon u_i)}{\partial x_i} = \frac{\partial}{\partial x_j}\left[\left(\mu + \frac{\mu_t}{\sigma_\varepsilon}\right)\frac{\partial \varepsilon}{\partial x_j}\right] + C_{1\varepsilon}\frac{\varepsilon}{k}(G_k + C_{3\varepsilon}G_b) - C_{2\varepsilon}\rho\frac{\varepsilon^2}{k} - R_\varepsilon$$

(A.7)

where G□ represents the generation of turbulent kinetic energy due to mean velocity gradients, G_β is the generation due to buoyancy, and Rε is an additional strain rate term in the RNG model.

A.3.2 Radiation and Discrete Phase Modeling

Solar radiation transfer was simulated using the Solar Ray Tracing algorithm in conjunction with the Discrete Ordinates (DO) method. The radiative transfer equation is expressed as:

$$\nabla \cdot (I\vec{s}) + (a + \sigma_s)I = an^2\frac{\sigma T^4}{\pi} + \frac{\sigma_s}{4\pi}\int_0^{4\pi} I(\vec{s'})\Phi(\vec{s}\cdot\vec{s'})d\Omega'$$

(A.8)

where I is the radiation intensity, s⃗ is the direction vector, a is the absorption coefficient, σ□ is the scattering coefficient, n is the refractive index, σ is the Stefan-Boltzmann constant, T is temperature, and Φ is the phase function.

PM□.□ dispersion was modeled using the Discrete Phase Model (DPM) with Lagrangian

particle tracking. The equation of motion for individual particles is:

$$\frac{d\overrightarrow{u_p}}{dt} = F_D\left(\vec{u} - \overrightarrow{u_p}\right) + \vec{g}\frac{(\rho_p - \rho)}{\rho_p} + \vec{F}$$

(A.9)

where $\vec{u}$□ is the particle velocity, $\vec{u}$ is the fluid velocity, F_D is the drag force per unit particle mass, ρ□ is the particle density, and $\vec{F}$ represents additional forces including Saffman lift, pressure gradient, and thermophoretic forces.

The atmospheric absorption and scattering coefficients in the DO model vary dynamically with PM□.□ concentrations through user-defined functions (UDF), enabling two-way coupling between the thermal environment and particulate matter dispersion.

A.3.3 Solution Algorithm and Convergence Criteria

The pressure-based coupled algorithm was employed to achieve complete pressure-velocity coupling with enhanced convergence characteristics for complex urban flows. Spatial discretization employed second-order upwind schemes for all transport equations to minimize numerical diffusion while maintaining solution stability.

Convergence criteria required simultaneous satisfaction of multiple conditions:

- Scaled residuals below 10□□ for all governing equations
- Stability of monitored variables (temperature, velocity components, mean radiant temperature, turbulent kinetic energy, and dissipation rate) over a minimum of 500 iterations
- Mass flux balance across domain boundaries within 1% tolerance

A.3.4 Adaptive Mesh Refinement

Grid adaptation was performed every 300 iterations based on gradient-based refinement criteria for temperature, velocity magnitude, and PM□.□ concentration fields. The refinement thresholds are specified in Table A.3. This adaptive approach increased the total cell count from 31.12 to 32.12 million while improving the minimum orthogonal quality to 0.12.

Table A.3 Adaptive mesh refinement criteria

Field Variable	Gradient Range	Coarsening Threshold	Refinement Threshold
Velocity	5.09×10□□ ~ 35.59	0.01	10
Temperature	1.42×10□¹□ ~ 44.23	0.001	10
PM□.□ concentration	1.42×10□¹□ ~ 3.41×10□□	1×10□□	3×10□¹□

The convergence behavior of field variables under grid adaptivity is illustrated in Figure A.4, demonstrating progressive reduction in relative errors between successive adaptive iterations. Air temperature relative errors decreased from 0.53% to 0.27%, wind velocity errors reduced from 22.98% to 6.28%, while PM□.□ concentration errors, though larger due to the inherently discrete nature of particulate matter transport, decreased from 52.25% to 24.8%.

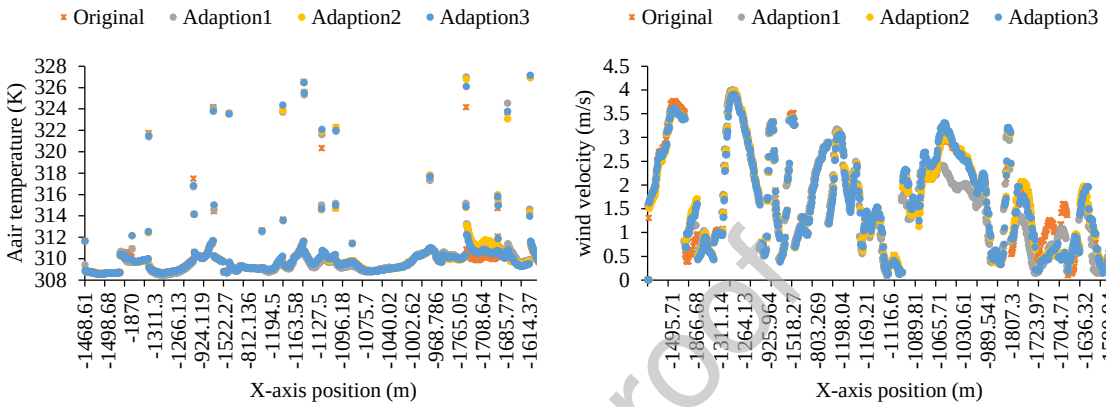

(a) Air temperature

(b) Wind velocity

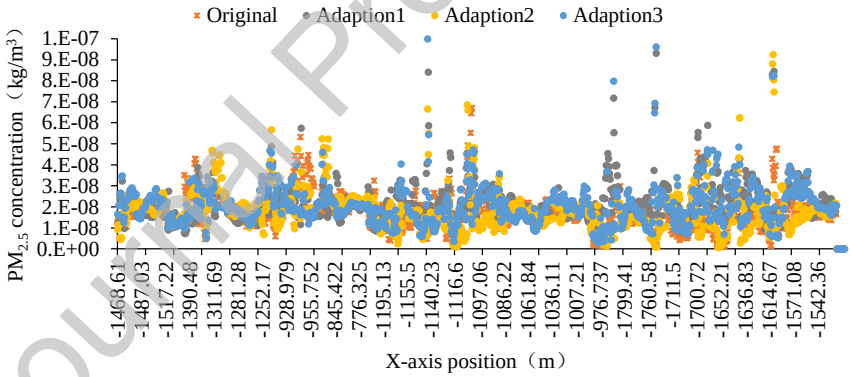

(c) $PM_{2.5}$ concentration

Figure A.4 Field variables under grid adaptivity: (a) Air temperature, (b) Wind velocity, (c) PM□.□ concentration

A.4 Model Validation Results

A.4.1 Temperature Validation

The thermal environment model was validated against field measurements collected at three

strategically positioned monitoring sites within the study domain. The temporal comparison between simulated and observed air temperatures is presented in Figure A.5. The model demonstrates robust predictive capability with coefficient of determination (R^2) values of 0.83, 0.78, and 0.82 for Sites A, B, and C respectively, overall mean absolute error (MAE) of 1.03°C, and root mean square error (RMSE) of 1.14°C.

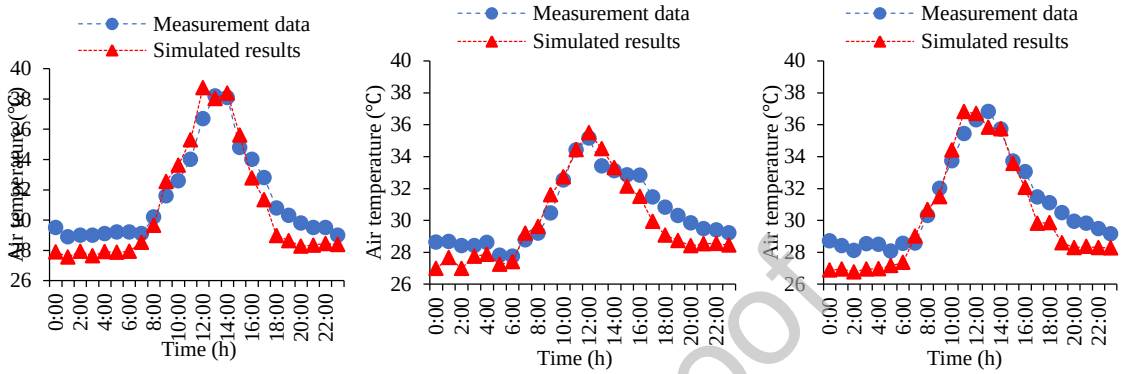

(a) Site A (b) Site B (c) Site C

Figure A.5 Comparison between simulated air temperature and measured values: (a) Site A, (b) Site B, (c) Site C

These accuracy metrics fall well within the acceptable range for urban thermal environment simulations, where published studies typically report MAE values between 1-4.36°C. The model exhibits systematic deviations with nighttime temperatures consistently underestimated (maximum deviation 1.89°C) and morning temperatures slightly overestimated (average error 0.76°C). These discrepancies are attributed to the steady-state modeling approach which does not capture thermal inertia effects in building materials and urban surfaces.

A.4.2 Wind Flow Validation

Wind speed validation results are presented in Figure A.6, demonstrating good agreement between simulated and measured values. The model achieves R^2 values of 0.81, 0.56, and 0.82 for Sites A, B, and C respectively, with an overall MAE of 0.08 m/s and site-specific MAE values of 0.10 m/s (Site A), 0.03 m/s (Site B), and 0.12 m/s (Site C).

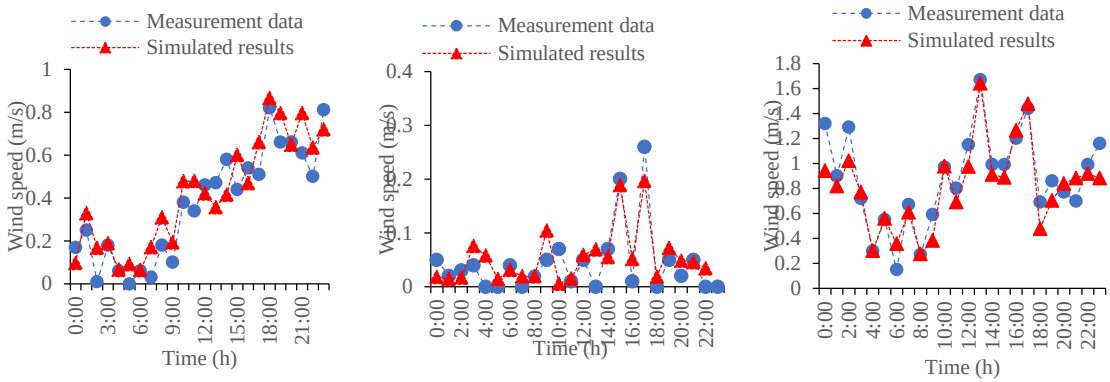

(a) Site A (b) Site B (c) Site C

Figure A.6 Comparison between simulated wind speed and measured values: (a) Site A, (b) Site B, (c) Site C

The model exhibits slight overprediction of wind speeds under low-wind conditions, particularly evident at Site B where the area experiences calm wind conditions throughout the diurnal cycle with average measured wind speeds of only 0.04 m/s. This discrepancy is attributed to simplified representation of building facade details and vegetation, which reduces wind resistance in the numerical model compared to actual conditions.

A.4.3 PM□.□ Concentration Validation

PM□.□ dispersion validation demonstrates the model's capability to accurately predict pollutant transport patterns within the urban environment, as illustrated in Figure A.7. The validation achieves R^2 values of 0.81, 0.71, and 0.83 for Sites A, B, and C respectively, with MAE values of 3.18, 7.20, and 5.11 μg/m³ for the respective sites, overall RMSE of 4.79 μg/m³, and relative errors of 15.71%, 19.55%, and 16.81%.

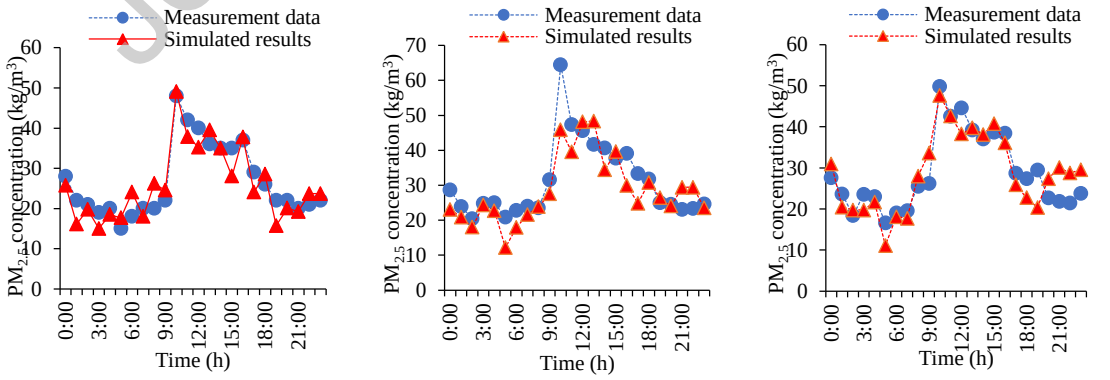

(a) Site A (b) Site B (c) Site C

Figure A.7 Comparison between simulated PM□.□ concentration and measured values: (a) Site A, (b) Site B, (c) Site C

These validation metrics compare favorably with published CFD-based PM□.□ studies, where relative errors frequently exceed 35% and absolute deviations can exceed a factor of two. The larger uncertainty in particulate matter predictions compared to continuous phase variables is inherent to the discrete nature of particle tracking methodologies and the complex interactions between turbulent dispersion and particle inertia.

A.5 Grid Independency

A systematic grid independence study was conducted employing three mesh densities: coarse (15 million cells), medium (31 million cells), and fine (47 million cells). Key output variables including area-averaged temperature, velocity magnitude, and PM□.□ concentration showed convergence with less than 3% variation between medium and fine mesh configurations, confirming adequate spatial resolution for the selected medium mesh.

A.6 Statistical Performance Metrics

Model performance was evaluated using standard statistical metrics commonly employed in urban environmental modeling:

Mean Absolute Error (MAE): $MAE = \frac{1}{n}\sum_{i=1}^{n}|P_i - O_i|$ (A.10)

Root Mean Square Error (RMSE): $RMSE = \sqrt{\frac{1}{n}\sum_{i=1}^{n}(P_i - O_i)^2}$ (A.11)

Coefficient of Determination (R²): $R^2 = 1 - \frac{\sum_{i=1}^{n}(O_i - P_i)^2}{\sum_{i=1}^{n}(O_i - \bar{O})^2}$ (A.12)

Index of Agreement (d): $d = 1 - \frac{\sum_{i=1}^{n}(O_i - P_i)^2}{\sum_{i=1}^{n}(|P_i - \bar{O}| + |O_i - \bar{O}|)^2}$ (A.13)

where P_i and O_i represent predicted and observed values respectively, $\bar{O}$ is the mean of observed values, and n is the total number of data points.

Declaration of interests

☒ The authors declare that they have no known competing financial interests or personal relationships that could have appeared to influence the work reported in this paper.

☐ The authors declare the following financial interests/personal relationships which may be considered as potential competing interests:

Graphical Abstract